Intensification of Tilted Tropical Cyclones Over Relatively Cool and Warm Oceans in Idealized Numerical Simulations

David A. Schecter[1]*

[1] *NorthWest Research Associates, Boulder, Colorado, USA*

Submitted to Journal of the Atmospheric Sciences February 22, 2021; Accepted November 4, 2021

DOI for the published journal article with final edits: 10.1175/JAS-D-21-0051.1.

*Corresponding author address: NorthWest Research Associates, 3380 Mitchell Lane, Boulder, CO, USA, 80301. E-mail: schecter@nwra.com

Abstract

A cloud resolving model is used to examine the intensification of tilted tropical cyclones from depression to hurricane strength over relatively cool and warm oceans under idealized conditions where environmental vertical wind shear has become minimal. Variation of the SST does not substantially change the time-averaged relationship between tilt and the radial length scale of the inner core, or between tilt and the azimuthal distribution of precipitation during the hurricane formation period (HFP). By contrast, for systems having similar structural parameters, the HFP lengthens superlinearly in association with a decline of the precipitation rate as the SST decreases from 30 to 26 ^{o}C. In many simulations, hurricane formation progresses from a phase of slow or neutral intensification to fast spinup. The transition to fast spinup occurs after the magnitudes of tilt and convective asymmetry drop below certain SST-dependent levels following an alignment process explained in an earlier paper. For reasons examined herein, the alignment coincides with enhancements of lower–middle tropospheric relative humidity and lower tropospheric CAPE inward of the radius of maximum surface wind speed r_m. Such moist-thermodynamic modifications appear to facilitate initiation of the faster mode of intensification, which involves contraction of r_m and the characteristic radius of deep convection. The mean transitional values of the tilt magnitude and lower–middle tropospheric relative humidity for SSTs of 28-30 ^{o}C are respectively higher and lower than their counterparts at 26 ^{o}C. Greater magnitudes of the surface enthalpy flux and core deep-layer CAPE found at the higher SSTs plausibly compensate for less complete alignment and core humidification at the transition time.

1. Introduction

The development of an incipient tropical cyclone into a mature hurricane has been studied extensively for decades. The basic objective is to understand how the spinup mechanism and intensification rate depend on environmental conditions and vortex structure. Theoretical and observational studies suggest that a positive correlation exists between the maximum possible intensification rate and the environmentally determined potential intensity of a tropical cyclone (e.g., Xu et al. 2016; Emanuel 2012). The potential intensity parameter depends on several factors, but generally increases over warmer oceans (e.g., Xu et al. 2019). There is also evidence that the time scales of genesis and post-genesis intensification of a tropical cyclone tend to grow with the magnitude of a theoretically-based ventilation index that increases with the ambient vertical wind shear and midlevel moisture deficit [Rappin et al. 2010 (RNE10); Tang and Emanuel 2012].

On the other hand, sizable spreads of intensification rates may be found among tropical cyclones in similar environments (e.g., Hendricks et. al 2010). One might reasonably ask how well the variability can be predicted by differences in a limited number of basic vortex parameters. The highest intensification rates in a particular environment are often observed when the maximum wind speed of the tropical cyclone is a moderate fraction of its empirical or theoretical potential (Xu and Wang 2015; Tang and Emanuel 2012). Observationally based statistical studies have also suggested a negative correlation between the intensification rate and the radius of maximum wind speed (Xu and Wang 2015,2018). On a related matter, observational and modeling studies suggest that the time scale required for an underdeveloped tropical cyclone to begin rapid intensification grows with the radius of maximum wind speed (Carrasco et al. 2014; Miyamoto and Takemi 2015).

Moreover, conventional wisdom maintains that a sufficiently large tilt of the tropical cyclone created by vertical wind shear or some other means will usually hinder the intensification process. The potential reasons are multifold. One proposed contributing factor

is the attendant warming of the lower–middle troposphere above the inner core of the surface vortex, tied to maintenance of nonlinear balance (DeMaria 1996). Another proposed contributing factor is the enhancement of "downdraft ventilation," whereby the tilt leads to an amplification of low-entropy downdrafts adulterating the boundary layer air that feeds inner core convection [e.g., Riemer et al. 2010,2013; Riemer and Laliberté 2015; Alland et al. 2021a (A21a)]. An appreciable tilt may also help reduce lower–middle tropospheric relative humidity over a broad central-to-uptilt section of the inner core of the surface vortex by (i) facilitating the lateral advection of dry external air into the region or (ii) facilitating subsidence of the entering airstream [e.g., Zawislak et al. 2016 (Z16); Alvey et al. 2020 (AZZ20); Schecter and Menelaou 2020 (SM20); Alland et al. 2021b]. The potential effects of introducing tilt stated above could directly weaken the convective activity driving intensification, or keep convection far (downtilt) from the center of the surface circulation, where it is plausibly less efficient in accelerating the maximum cyclonic winds [e.g., Vigh and Schubert 2009; Pendergrass and Willoughby 2009; Schecter 2020 (S20)].

Of paramount importance is to understand the mechanism and time scale by which an incipient tropical cyclone might overcome the foregoing detrimental effects of tilt and strengthen into a hurricane. One strategy for addressing this issue has been through simplified modeling studies of weak tropical cyclones exposed to steady environmental vertical wind shear on the f-plane [e.g., Nolan and Rappin 2008; RNE10; Rappin and Nolan 2012 (RN12); Tao and Zhang 2014 (TZ14); Finnochio et al. 2016; Onderlinde and Nolan 2016; Rios-Berrios et al. 2018 (RDT18); Gu et al. 2019]. The aforementioned studies have underscored the potential importance of "precession" in regulating the time scale of hurricane formation.[1] In the pertinent simulations, the tropical cyclone initially develops a downshear tilt in conjunction with downshear convection. The tilt vector (the vector difference between the midlevel and surface centers of rotation) then precesses in concert with the azimuthal propagation of

[1]While sometimes given a more restrictive definition, the term "precession" herein refers to rotation of the tilt vector over time by *any* adiabatic, diabatic or hybrid mechanism. Likewise, the term "alignment" refers to contraction of the tilt vector by any means.

convection toward the upshear semicircle. A transition to fast alignment and spinup tends to occur once the angle of the tilt vector measured cyclonically from the shear vector increases to or beyond the neighborhood of 90^o (e.g., RN12; TZ14; RDT18). The relative importance of various kinematic and thermodynamic changes— coinciding with the reorientation of tilt —for the onset of fast alignment and spinup is a topic of ongoing research (ibid.; see also Chen and Gopalakrishnan 2015). One basic and seemingly important change is the nullification (or reversal) of the shear-induced misalignment forcing (e.g., Reasor et al. 2004).

Among the simplified modeling studies mentioned above, there have been a number of sensitivity tests involving variation of environmental parameters. TZ14 notably showed that raising the SST from 27 to 29 ^{o}C without adjusting the initial environmental sounding toward one of radiative convective equilibrium (cf. Nolan and Rappin 2008; RNE10) expedites the transformation of a sheared (tilted) tropical cyclone into a hurricane. Such a result is intuitively reasonable based on the elevated level of moist-entropy allowed near the surface, and the related expectation of enhanced diabatic forcing to support the lower-to-middle tropospheric convergence of angular momentum that leads to intensification (further discussed by Črnivec et al. 2016). Adding to this, warming the ocean (in TZ14) appears to improve the efficiency of diabatic alignment processes in reducing tilt from an early stage of the tropical cyclone's evolution. Such reduction of the tilt magnitude can limit the early detrimental impacts of misalignment, and accelerate the precession that brings forth a transition to fast spinup (TZ14; Schecter 2016; RDT18).

Schecter and Menelaou (SM20) introduced a distinct line of idealized cloud resolving modeling studies in which vertical wind shear is virtually eliminated from the environment of an initially tilted tropical cyclone. Such a setup was designed to address theoretical questions, but may have some direct relevance to situations in nature where tropical cyclones exposed to minimal shear have lingering tilts from prior forcing. SM20-type simulations are specifically intended to provide clear pictures of how tilt alone alters the organization of convection and the intensification rate. They are also intended to elucidate the efficiency of intrinsic

alignment mechanisms in diminishing the detrimental impact of a tilt created in the past. The preceding issues are not adequately resolved by studies preceding SM20 in which tilt coexists with an everlasting environmental shear-flow. The shear-flow clouds the picture by potentially enhancing ventilation and altering surface fluxes. Moreover, a sufficiently strong dynamical coupling of tilt with the shear-flow can fundamentally change the pathways of alignment and intensification. Whereas reorientation of the tilt vector through precession can be critical to enabling the onset of fast alignment and spinup when shear is present, reorientation of the tilt vector is irrelevant in a quiescent environment.

The numerical simulations of SM20 expectedly showed that initial tilt magnitudes exceeding the core radius of a tropical cyclone appreciably hinder its transformation into a hurricane. Of greater note, increasing the initial tilt magnitude to several times the core radius was found to extend the hurricane formation period (defined in section 3a) by an order of magnitude. A Sawyer-Eliassen based analysis explicitly showed how the positive spinup tendency formally attributable to diabatic processes has trouble dominating the net negative tendency associated with other factors such as friction when a tropical cyclone is strongly misaligned. This condition of frustrated spinup generally ends upon sufficient decay of the tilt magnitude. SM20 analyzed various mechanisms working to reduce tilt, but did not thoroughly investigate the amount of alignment and other changes to the system required for a substantial boost of the intensification rate. Moreover, SM20 focused exclusively on systems with an SST of 28 ^{o}C. A broader survey is necessary given the sensitivities of tilt dynamics and vortex intensification to variation of the SST that have been demonstrated by related studies incorporating vertical wind shear (e.g., TZ14).

The present study is essentially a continuation of SM20. Changes to the relationship between the initial tilt magnitude and the time scale of hurricane formation caused by warming or cooling the underlying ocean will be examined. The effects of changing the SST on the relationships between tilt, the core radius and the spatial distribution of precipitation will also be investigated. Tilt-related thermodynamic impediments to intensification common

among tropical cyclones over the full range of SSTs considered herein will be illustrated and explained; the main distinction from earlier illustrations will be in the removal of modulation by environmental vertical wind shear. Perhaps the most novel contribution of this paper will lie in an effort to quantify the reduction of tilt and attendant thermodynamic structural changes needed for an initially misaligned tropical cyclone to transition from a state of slow to fast spinup. This effort will notably reveal how changing the SST affects the requirements for such a transition to occur.

Before moving on, it is important to acknowledge the possibility of circumstances under which an initial misalignment could actually serve as a catalyst for spinup by stimulating strong downtilt convection (e.g., Jones 2000). Initially, convective activity far from the surface vortex center may not be optimal for spinup, but sufficiently strong convection concentrated downtilt could create a smaller vorticity core that quickly intensifies and soon dominates the parent cyclone. Analogous "core reformation" events involved in the rapid intensification of systems with moderate environmental vertical wind shear have been discussed at length in the literature (e.g., Nguyen and Molinari 2015; Chen et al. 2018). One might speculate that increasing the SST beyond some threshold in an SM20-type simulation could set the stage for downtilt convection that is sufficiently vigorous to reverse the otherwise negative influence of tilt on intensification. However, this fails to occur for the systems considered herein— which have SSTs ranging up to 30 ^{o}C —and will therefore not be among the topics addressed below.

The remainder of this article is organized as follows. Section 2 explains the setup of the numerical simulations. Section 3 provides a basic overview of hurricane formation in the entire simulation set. Included in the overview is a discussion of how variation of the SST affects the growth of the time scale of hurricane formation with increasing values of the initial tilt magnitude. Section 4 takes a moment to show that the delay of hurricane formation caused by a large initial tilt far exceeds that which would be caused solely by the attendant early modification of the symmetric component of the tropical cyclone that is theoretically

detrimental on its own. Section 5 examines details of the thermodynamic impediments to intensification that are common among the tilted tropical cyclones considered herein before the onset of fast spinup. Section 6 examines the structural changes that signal an imminent transition to fast spinup at various SSTs. Section 7 summarizes the findings of this study.

2. Methodology

2.a Model Configuration

The evolutions of weak tropical cyclones into hurricanes are simulated herein with release 19.5 of Cloud Model 1 (CM1; Bryan and Fritsch 2002). As in SM20, the model is configured with a variant of the two-moment Morrison microphysics parameterization (Morrison et al. 2005,2009), having graupel as the large icy-hydrometeor category and a constant cloud-droplet concentration of 100 cm^{-3}. The influence of subgrid turbulence above the surface is accounted for by an anisotropic Smagorinsky-type closure that is tailored for tropical cyclone simulations as explained in SM20. Surface fluxes are parameterized with bulk-aerodynamic formulas. The momentum exchange coefficient C_d increases with the surface wind speed from 10^{-3} to 0.0024 above 25 m s^{-1} (compare with Fairall et al. 2003 and Donelan et al. 2004). The enthalpy exchange coefficient is given by $C_e = 0.0012$ roughly based on the findings of Drennan et al. (2007). Heating associated with frictional dissipation is activated. Rayleigh damping is imposed above an altitude of $z = 25$ km. The model is computationally and physically simplified by eliminating radiative transfer. There is ample evidence in the literature that realistically distributed radiation tends to accelerate tropical cyclone development (e.g., Rios-Berrios 2020; Ruppert et al. 2020). Nevertheless, we provisionally assume that the simplified model captures the essential features of tilted tropical cyclone dynamics.

All simulations are conducted on a doubly periodic oceanic f-plane with a Coriolis parameter of 5×10^{-5} s^{-1}. The SST is held constant in space and time. The simulations are separated into three groups distinguished by whether the SST is 26, 28 or 30 ^{o}C. In the same

order, these three groups will be called T26, T28 and T30. Ambient vertical wind shear is reduced to a negligible level after the tropical cyclones are misaligned (see section 2b).

The equations of motion are discretized on one of two stretched rectangular grids having relatively low resolution (LR) or high resolution (HR). All simulations from SM20 that are incorporated into the present study use the HR grid. The majority of new simulations use the LR grid for computational efficiency. Differences between LR and HR simulations seem limited to contextually unimportant details. In either case, the grid spans 2,660 km in both horizontal dimensions, and extends upward to $z = 29.2$ km. The 800×800 km^2 central region of the horizontal mesh has uniform increments of 2.5 (1.25) km in the LR (HR) simulations. At the four corners of the mesh, the LR (HR) increments are 27.5 (13.75) km. In the vertical, the LR (HR) grid has 40 (73) levels. For the LR (HR) grid, the spacing between levels increases from 0.1 to 0.7 to 1.4 (0.05 to 0.4 to 0.75) km as z increases from 0 to 8 to 29 km.

2.b Initialization

Before describing the initialization and evolution of a tilted tropical cyclone, several notational conventions should be established. In this paper, r, φ and z will always be used to represent (in order) the radius, azimuth and height above sea level in a *surface vortex centered* cylindrical coordinate system. Time will be represented by t. The variables u, v and w will respectively represent the radial, azimuthal and vertical velocity fields. Furthermore, an overline over an arbitrary fluid variable will denote an average of that variable over φ.

The tilted vortices in all simulations are derived from a vertically aligned incipient tropical cyclone that developed over a 99-h period from a weaker system in a shear-free environment with an SST of 28 ^{o}C and an initial thermodynamic profile matching that of the Dunion (2011) moist tropical sounding in the far field. Interested readers may consult SM20 (Fig. 2 therein) for a detailed depiction of the kinematic and moist-thermodynamic structure of the basic state of this *root vortex*. Here we summarize only its most salient features. The basic state of the root vortex has an azimuthal velocity field $\bar{v}$ maximized

at 12.0 m s^{-1} at $r = 115.1$ km and $z = 3.7$ km. The surface maximum of $\bar{v}$ (denoted v_m) is 8.6 m s^{-1} at a radius (denoted r_m) of 42.9 km. The decay of $\bar{v}$ beyond r_m (on the surface) is relatively slow, in dropping by only 30% out to $r = 254$ km. The outer extremities of the primary and secondary circulations are roughly 10^3 km away from the center of rotation. Of further note, much of the inner core has relative humidity of 89-100%, meaning that the system is well primed for quasi-symmetric intensification barring any detrimental disturbance (e.g., Nolan 2007).

Before each simulation starts in earnest, the SST is adjusted (if necessary) to its group value without modifying any other aspect of the environment. Moreover, the root vortex is transformed into a tilted vortex using one of the three procedures that are thoroughly explained in SM20 (section 2a and appendix A therein). Implementation of several procedures over the simulation set is deemed beneficial in creating some variability of early convection and structural detail among systems with comparable initial misalignments, which may reduce potential bias in the presented results. The three tilting procedures are called the impulsive separation (IS), impulsive separation plus damping (ISPD), and dry separation plus damping (DSPD) methods. Each method creates a tilt by imposing a transient environmental shear-flow that horizontally separates the upper and lower sections of the vortex that lie above and below a km-scale transition layer centered at height z_l, which is usually set to 5.25 km. The degree of horizontal separation (tilt) is determined by the strength and duration of the shear-flow. For simulations that implement the IS or ISPD method, the forcing that turns the shear-flow on and off is "impulsive" in lasting only 6 hours. The ISPD method ends with a brief period of damping of the minimal domain-averaged winds that may unintentionally exist after the tilt is generated. Importantly, moist convection is allowed to stay active while the vortex is tilted when using either the IS or ISPD method. The DSPD method is similar to its ISPD counterpart in adding a brief period of corrective damping after the forcing ends, but the forcing can be longer and weaker. Moreover, moist convection is temporarily deactivated by removing hydrometeors and replacing water vapor

with a passive tracer. When the procedure ends, moist convection is reactivated by changing the passive tracer back into water vapor, and t is reset to zero. Regardless of the method used, the initial tilting reduces relative humidity above the inner core of the surface vortex, and causes a convectively driven enlargement of r_m during or shortly after implementation.[2]

2.c Working Definition of the Tilt Vector

The initial and subsequent misalignment of a tropical cyclone is quantified by the tilt vector. The tilt vector is defined by $\mathbf{x}_{cm} - \mathbf{x}_{cs}$, and its magnitude is denoted by *tilt*. As in SM20, $\mathbf{x}_{cs}$ and $\mathbf{x}_{cm}$ represent the centers of rotation of the cyclonic circulations in thin layers adjacent to the sea-surface (subscript *cs*) and in the middle troposphere (subscript *cm*). The surface-adjacent layer extends up to $z = 1.0$ (1.2) km, and the middle tropospheric layer spans the interval $7.3 \leq z \leq 8.1$ ($7.1 \leq z \leq 8.5$) km for HR (LR) simulations. Each center of rotation precisely corresponds to the point at which one must place the origin of a polar coordinate system to maximize the peak value of $\bar{v}$ in the pertinent layer. Interested readers may consult section 2b of SM20 for details of the center finding algorithm. In doing so, note that the spacing of the fine grid used to find $\mathbf{x}_{cs}$ or $\mathbf{x}_{cm}$ (the value of l_f given therein) is doubled for analyzing the LR simulations in this paper.

2.d Tabulated Synopsis of the Constituent Members of Each SST Group

For convenient reference, Table 1 summarizes the simulations considered for this study. As noted earlier, the simulations are separated into three groups according to their SST. Each SST group contains 9-11 LR simulations, but only T28 (which includes SM20 data)

[2] A few details omitted from the preceding discussion should be noted. In contrast to all other simulations, eight of the HR simulations in group T28 split the vortex at $z_l = 3.5$ or 1.75 (as opposed to 5.25) km. All but one of the HR simulations in group T28 are taken directly from SM20; these include the control run and the 21 tilted tropical cyclone simulations described in Table 1 therein. A variant of the minimal-tilt control run of SM20 is repeated here, starting with an axisymmetrized version of the root vortex (the *a-root* vortex) that includes the water vapor distribution but excludes the secondary circulation and all hydrometeors. The same initial condition is used for the T26, T28-LR and T30 simulations with zero initial tilt. Moreover, the ISPD procedure of SM20 has been slightly modified for the new LR simulations by replacing the unfiltered root vortex with the a-root vortex prior to tilting.

contains more than a few HR simulations. The initial tilt magnitude ($tilt_0$) ranges from 0 to approximately 370 km in all SST groups.[3] The rightmost columns of the table briefly describe and name the "featured" members of each SST group that will be selected for detailed analysis in various sections of the paper. The description contains the value of $tilt_0$, and the time averages of *tilt* and r_m (denoted by triangular brackets) over the hurricane formation period to be defined in section 3a. The suffix in the name of any particular group member indicates the resolution of the simulation (LR or HR), and is terminated by a letter (A or B) that differentiates one LR or HR simulation from another. While not of critical importance, all featured simulations are initialized using the DSPD tilting procedure with $z_l = 5.25$ km. Time averages of *tilt* and r_m are not given for T26-HRA, because in contrast to all other simulations, the tropical cyclone fails to complete hurricane formation within its 500-h duration. While T26-HRA will be incorporated into the discussions of section 5 and appendix C (Fig. C1a), it will be excluded from the analyses of all other sections.

3. Overview of the Simulations

3.a Time Scale of Hurricane Formation versus Initial Tilt, Core Size, and the SST

As in SM20, the hurricane formation period (HFP) is defined as the time interval during which the surface maximum of the φ-averaged tangential velocity (v_m) intensifies from 12.5 to 32.5 m s^{-1}. The length of the HFP will be denoted $\tau_{\rm hf}$, and the time average of an arbitrary variable h over the HFP will be represented by the expression $\langle h \rangle$. It is worth remarking that because v_m differs from the conventionally defined maximum sustained surface wind speed of a tropical cyclone, the endpoint of the HFP does not precisely correspond to when an asymmetric hurricane would be officially declared.

Figure 1a demonstrates that $\tau_{\rm hf}$ increases with $tilt_0$, when the value of $tilt_0$ exceeds the

[3]To be precise, $tilt_0$ is the maximum tilt magnitude measured during the interval $0 \le t \le 6$ h, in which $t = 0$ corresponds to the start of the 6-h impulsive IS or ISPD tilting procedure, or the end of the generally non-impulsive DSPD procedure.

initial 100-km radial length scale of the core of the tropical cyclone. As noted in section 1, there is some theoretical basis for believing that the HFP should lengthen as the characteristic radius of convection increases. The positive correlation between $\tau_{\rm hf}$ and $tilt_0$ may therefore be a reflection of greater initial tilts leading to greater outward displacements of the dominant convective activity within a tropical cyclone. Because convection is statistically peaked near r_m in the systems under consideration (SM20 and section 3b), moving convection outward generally coincides with creating a larger vortex core. Figure 1c verifies that the core size during hurricane formation tends to increase with the initial tilt magnitude when the latter exceeds roughly 100 km. Figure 1b shows how the growth of $\tau_{\rm hf}$ with increasing $tilt_0$ translates into the growth of $\tau_{\rm hf}$ with increasing $\langle r_m \rangle$ in each SST-group.

Figure 1b further shows that $\tau_{\rm hf}$ tends to grow with decreasing SST at a given value of $\langle r_m \rangle$. Moreover, whereas [for moderate-to-high values of $\langle r_m \rangle$] the length of the HFP increases on the order of 10 h from group T30 to T28, the length of the HFP increases on the order of 100 h from group T28 to T26.

Figure 2 suggests that the root cause for prolonged development over cooler oceans is a reduction of the diabatic forcing— reflected in a reduction of the precipitation rate —that drives intensification. Herein, the local precipitation rate $P(r, \varphi, t)$ is calculated from the local surface rainfall accumulated over a 2-h period centered at t. The *area-integrated precipitation rate* within a surface vortex centered disc of radius r is given by

$$\mathcal{P}_I(r,t) \equiv \int_0^{2\pi} d\varphi \int_0^r d\tilde{r}\tilde{r} P(\tilde{r}, \varphi, t). \tag{1}$$

Figure 2a shows the mean and spread of $\langle \mathcal{P}_I \rangle$ for each SST group. It is seen that decreasing the SST (i) reduces the area-integrated precipitation rate within a 150-200 km scale disc that generally incorporates the broader core region of the tropical cyclone during the entire HFP, and (ii) reduces the radial extent of precipitation indicated by where the $\langle \mathcal{P}_I \rangle$-curve levels off.[4]

Further analysis reveals that the highly nonlinear growth of $\tau_{\rm hf}$ with decreasing SST

[4]Lin et al. (2015) reports a similar observational dependence of tropical cyclone precipitation on relative SST.

for any sufficiently large value of $\langle r_m \rangle$ (Fig. 1b) coincides with a highly nonlinear decay of the area-integrated precipitation rate in a disc bounded (approximately) by the maximum surface winds of the tropical cyclone. Figure 2b shows the $\langle r_m \rangle$-dependence of $\langle \mathcal{P}_I(a,t) \rangle$, in which the time-dependent disc radius is given by $a = 1.2\, r_m(t)$. The T30 and T28 data points are seen to closely follow a common linear regression. The $\langle \mathcal{P}_I \rangle$ data from group T26 clearly diverge from this linear trend and virtually level off beyond $\langle r_m \rangle \approx 40$ km. The result at larger values of $\langle r_m \rangle$ is a sizable reduction of the time-averaged area-integrated precipitation rate relative to that found in the inner cores of tropical cyclones over the two warmer oceans. It is worth remarking that the values of $\langle \mathcal{P}_I \rangle$ in Fig. 2b are tightly correlated to the inward mass current at r_m in the boundary layer of the tropical cyclone, as represented by the variable $-\langle r_m(t)\, \bar{u}[r_m(t), t] \rangle$, in which $\bar{u}$ is vertically averaged over a 1-km layer adjacent to the sea-surface. Including data from all SST groups, the Pearson correlation coefficient is 0.99.

3.b Basic Structural Similarities of Tilted Tropical Cyclones at all SSTs

Despite differences in the precipitation rates found over relatively cool and warm oceans (Fig. 2), several basic structural features of the developing tropical cyclones do not vary much with the SST. Figure 3a shows a fairly insensitive positive linear relationship between the HFP time averages of the tilt magnitude and r_m when both variables exceed 35 km. The minor displacement of all T30 tilt magnitudes above the plotted regression line in this parameter regime is notable, but of questionable importance given that two of the T26 data points have comparable upward shifts. Figure 3b shows that there is also an insensitive positive linear relationship between the HFP time averages of the precipitation radius r_p and r_m. As in SM20, r_p is the radius from the surface vortex center at which the φ-averaged precipitation rate $\bar{P}$ is maximized. The value of $\langle r_p \rangle$ typically exceeds $\langle r_m \rangle$ by 5-10 km.

Figure 3c shows a generic r-t Hovmöller plot of $\bar{P}$, and further illustrates the fairly tight coupling between the radius of peak precipitation and the radius of maximum wind

speed (white line) during the HFP. The superimposed black contours correspond to the azimuthal average of w_+ evaluated at $z = 8$ km, in which $w_+ = w$ (0) where the vertical velocity w is greater than (less than) $w_c = 5$ m s^{-1}. The contours help verify that r_p tends to be near the radius r_w where $\overline{w_+}$ is peaked and deep convection is prominent. A more comprehensive analysis of time averaged quantities including data from all SST groups yields the linear regression $\langle r_w \rangle = 13.6 + 0.89 \langle r_p \rangle$ (in km) with an associated correlation coefficient of 0.97.[5]

Of additional note, changing the SST has no major consequence on the relationship between the tilt and the azimuthal distribution of P. For illustrative purposes, Fig. 4a shows a snapshot of the asymmetric precipitation rate existing within a moderately tilted tropical cyclone. Lower and middle tropospheric streamlines are superimposed on the plot to convey the horizontal separation of rotational centers defining the tilt vector. It is clear that P is mostly concentrated downtilt, similar to what is commonly seen in nature [e.g., Stevenson et al. 2014; Nguyen et al. 2017 (NRR17)].

Figure 4b shows the precipitation probability distribution (PPD) versus the time averaged tilt magnitude during the HFP for all simulated systems. The precipitation probability is distributed over four equal quadrants of a circular disc of radius a centered at $\mathbf{x}_{cs}$. The four quadrants used for the present analysis are depicted with distinct colors in the inset. They are centered at $\varphi = 0$, $\pi/2$, π and $3\pi/2$ radians, in which $\varphi = 0$ corresponds to the time-dependent direction of the tilt vector. The precipitation probability in the quadrant centered at φ is defined by $\langle \hat{\mathcal{P}}_\varphi \rangle$, in which

$$\hat{\mathcal{P}}_\varphi(t;a) \equiv \int_{\varphi-\pi/4}^{\varphi+\pi/4} d\tilde{\varphi} \int_0^a dr r P(r,\tilde{\varphi},t) \Big/ \mathcal{P}_I(a,t). \tag{2}$$

In other words, the precipitation probability is the HFP time average of the integral of

[5]Sensitivity tests with w_c raised to 10 m s^{-1} or with w_+ evaluated at $z = 4$ km (and w_c varied between 2.5 and 5 m s^{-1}) consistently produced values of $\langle r_w \rangle$ fairly close to $\langle r_p \rangle$. Regarding technical procedures, the search for r_w is restricted to $r < 3r_m$, and the time average of r_w is computed excluding occasional brief intervals in which w (at the evaluation height) is less than w_c everywhere in the search region. Moreover, HR simulation data is locally averaged onto the LR grid before computing w_+.

the precipitation rate over the area of quadrant-φ divided by the integral over the entire disc. The plotted probabilities are evaluated with $a = 200$ km to account for most of the precipitation within the relatively large cores of strongly tilted vortices. It is seen that there is minimal variation of the PPD with the SST for small and medium tilt magnitudes. In general, the downtilt ($\varphi = 0$) probability rapidly grows at the expense of its uptilt and lateral counterparts as the tilt magnitude increases from 20 to 60 km. Over this interval, the systems change from having statistically symmetric precipitation to having roughly 60 percent of the precipitation occurring downtilt. As the tilt magnitude increases beyond 60 km, the PPD for group T28 stays fairly constant. There is some hint that the T26 (T30) PPDs may become modestly more symmetric (asymmetric), but a definitive statement on the matter would require a greater number of large-tilt data points.[6]

4. Dynamical Importance of the Tilt-Related Structural Asymmetry of a Tropical Cyclone

The preceding overview did not directly answer whether the structural asymmetry of the tropical cyclone associated with tilt is critical to impeding hurricane formation once the HFP officially begins. The answer is not entirely obvious, partly because systems with the largest tilt magnitudes tend to have the largest values of r_m at the start of the HFP,[7] and the developmental time scale tends to increase with the initial value of r_m even in axisymmetric models (e.g., Rotunno and Emanuel 1987). The additional detriment of tilt to intensification can be verified for any particular case, if faster spinup can be shown to occur after restarting the simulation with only the symmetric component of the vortex. The following considers such restarts for simulations T26-LRA, T28-LRA and T30-LRA at the beginning of the

[6]It should be noted that the PPD varies to some extent with the disc radius a. Repeating the preceding analysis with $a = 1.2r_m$ increases the HFP time averaged precipitation probability in the $\varphi = \pi/2$ (downwind of downtilt) quadrant mostly at the expense of that in the $\varphi = 3\pi/2$ (upwind of downtilt) quadrant, but does not introduce any notable differences between the SST groups. The $\varphi = 0$ (downtilt) precipitation probability gains dominance over its $\varphi = \pi/2$ counterpart (and all others) as $\langle tilt \rangle$ increases beyond approximately 40 km.

[7]Considering systems with $tilt_0 > 100$ km, the correlation coefficients between $tilt_0$ and r_m averaged over the first 6 hours of the HFP are 0.81 for group T26, 0.79 for group T28, and 0.88 for group T30.

HFP ($t = t_b$), when the tilt magnitudes are substantial and convective asymmetries are pronounced.[8] The symmetric vortices in the restarts are obtained from the azimuthally averaged fields of the tilted tropical cyclones in a surface vortex centered coordinate system. Whereas the symmetric component of the water vapor mixing ratio is retained, hydrometeors are removed.

Figure 5 compares the evolutions of the surface azimuthal velocity fields in the tilted and symmetrized systems. The surface vortices of the tilted tropical cyclones retain their broad structures and slowly intensify. The intensification of outer winds actually outpaces that found in the symmetrized restarts. However, the inner core of each symmetrized tropical cyclone shortly enters a stage of faster spinup, coinciding with contraction of r_m and r_p. Faster spinup of the inner core obviously implies a shorter HFP.

Figure 6a shows $\tau_{\rm hf}$ plotted against $\langle r_m \rangle$ for the tilted systems (filled symbols) and their symmetrized counterparts (empty symbols). The reductions of $\tau_{\rm hf}$ resulting from symmetrization are seen to coincide with considerable reductions of $\langle r_m \rangle$. Of note, the value of $\tau_{\rm hf}$ for each symmetrized system falls roughly two root-mean-square deviations below the $\tau_{\rm hf}$ versus $\langle r_m \rangle$ regression line obtained for tilted vortices at the same SST. It stands to reason that the regressions are quantitatively unreliable when r_m is not dynamically coupled to a misalignment. Note also that the data shown here (and in Figs. 6b-d) for the tilted systems do not appreciably change when hydrometeors are removed at $t = t_b$, as in the symmetrized restarts, without modifying any other fields. Such insensitivity should allay concerns raised during peer review that removing hydrometeors at the restart-time could be more important than symmetrization in altering the basic statistics of hurricane formation.

Moving on, Figs. 6b-d convey various changes of precipitation and low-level inflow between the tilted tropical cyclone simulations and the symmetrized restarts. Figure 6b compares time averages of the precipitation asymmetry, defined by

[8]The values of t_b are 18.2 , 25.1 and 31.0 h for simulations T30-LRA, T28-LRA and T26-LRA, respectively. For all simulations in Table 1, t_b ranges from 6.6 to 66 h.

$$P_{asym}(t;a) \equiv \sqrt{\frac{4}{3}\sum_{\varphi}\left(\hat{\mathcal{P}}_{\varphi}(t;a)-\frac{1}{4}\right)^2}, \tag{3}$$

in which $\hat{\mathcal{P}}_{\varphi}$ is given by Eq. (2), $\varphi-\varphi_b \in \{0, \pi/2, \pi, 3\pi/2\}$, and φ_b is chosen so as to maximize the sum over φ on the right-hand side. By construction, $P_{asym} = 0$ when the precipitation is uniform and $\hat{\mathcal{P}}_{\varphi} = 1/4$ for all φ, whereas $P_{asym} = 1$ when all precipitation occurs in one quadrant. Large symbols in the figure represent averages taken over the HFPs of the tilted tropical cyclone simulations and the symmetrized restarts. Small filled symbols, connected by thin lines to their larger counterparts, represent averages of the tilted-system variables taken over the shorter HFPs of the symmetrized restarts (the time periods in Fig. 5). The ordinate and abscissa of the graph respectively correspond to P_{asym} measured with the disc radius a equal to $1.2r_m(t)$ and 200 km. The graph verifies that the precipitation fields within either the inner or broader cores of the initially symmetrized systems develop minimal statistical asymmetry compared to that found in the tilted systems.

Figure 6c is similar to 6b but for the area-integrated precipitation rate $\mathcal{P}_I(a,t)$ [Eq. (1)] with the two values of a stated previously. In general, symmetrization does not cause a major boost of the area-integrated precipitation rate— which can be viewed as an indirect measure of latent heat release —over the inner or broader core of the surface vortex. The symmetrized restart of the T28 simulation only modestly violates this rule in causing a 14-16% boost of both variants of $\mathcal{P}_I$ over the time-period in Fig. 5. Symmetrization more consistently reduces the magnitude of the time averaged inward mass-flux $(-r\bar{u})$ in the 1-km deep boundary layer at both $r = 1.2r_m(t)$ and 200 km (Fig. 6d). So, there is no compelling evidence that faster spinup in the restarts generally results from augmented convection, despite the possibility of tilt removal diminishing a potentially destructive downflux of low-entropy air into the lower tropospheric inflow (e.g., Riemer et al. 2010,2013; Riemer and Laliberté 2015; A21a).

In summary, without necessarily decreasing the average precipitation rate over the broader core of the surface vortex, or the inward mass-flux in the 1-km deep boundary layer, the existence of tilt at an early stage of development can effectively disable a relatively efficient

intensification process that is found in our quasi-symmetric tropical cyclones.[9] The tilt lingers as an integral part of an asymmetric tropical cyclone structure that evidently hinders the contraction of r_m and r_p. Hindering contraction of the inner core and inward migration of deep convection is believed to render the diabatic forcing less effective in supporting fast spinup of cyclonic winds in the lower troposphere during the HFP (see for example, S20; Pendergrass and Willoughby 2009).

5. Detailed Structure of a Tilted Tropical Cyclone During Slow Intensification

A common feature of tilted tropical cyclone development in our simulations is a transition from slow to fast intensification prior to the emergence of a hurricane. As one might expect from the foregoing results, substantial reduction of the tilt magnitude is a common precursor of the transition (see section 6). To fully comprehend why a moderate-to-strong tilt tends to prevent fast spinup requires an understanding of the relationship between tilt and the internal moist-thermodynamic state of a tropical cyclone. This relationship is expounded below for simulations T30-HRA, T28-HRA and T26-HRA. The tropical cyclone in T28-HRA is selected for detailed examination for continuity with a complementary analysis of the same system in SM20, where the simulation is named DSPD-X400Z5. The other systems are selected because of their similar resolutions and initial conditions, but distinct SSTs.

Figure 7 displays 6-h time averages of the velocity fields and moist-thermodynamic structures of the tilted tropical cyclones under present consideration when at moderate tropical storm intensity, before any potential transition to fast spinup. The start time of each averaging period will be denoted t_s for future reference. In all cases, the misalignments of streamlines in the boundary layer and middle troposphere (left column of Fig. 7) are substantial, but appreciably reduced from their initial magnitudes. Consistent with the time averaged precipitation statistics presented in section 3b, the strongest upper tropospheric

[9]This process is presumably akin to that of other vertically aligned systems reviewed elsewhere (e.g., Montgomery and Smith 2014).

updrafts associated with deep convection (middle column) are concentrated downtilt near the radius of maximum surface wind speed. The moist-thermodynamic fields (middle and right columns) are not identical to each other, but have some common features that seem to resemble those found in earlier observational studies of tilted tropical cyclones [e.g., Dolling and Barnes 2012 (DB12); Reasor et al. 2013; Z16; NRR17]. The following examines the most notable features that are believed to help keep convection far downtilt from the surface vortex center, where it is theoretically inefficient in driving intensification.

5.a Lower–Middle Tropospheric Relative Humidity

Compared to conditions downtilt, the values of lower–middle tropospheric relative humidity uptilt and near the surface vortex center are fairly low (see Figs. 7c, 7f and 7i). There is longstanding evidence that low relative humidity above the boundary layer in combination with weak-to-moderate deep-layer CAPE (applicable to our systems) hinders deep convection by the dilution of updrafts if nothing else (e.g., Brown and Zhang 1997; James and Markowski 2010; Kilroy and Smith 2013; Tang et al. 2016). It stands to reason that the aforementioned relative humidity deficits help limit the invigoration of deep convection in the central and uptilt regions of the tropical cyclones under present consideration.

Figure 8 illustrates the moisture dynamics (in an earth-stationary reference frame) maintaining the central and uptilt lower–middle tropospheric relative humidity deficits for the representative case of simulation T28-HRA. All fields are averaged over the 6-h time period connected to Figs. 7d-f. Figures 8a and 8b are reference plots superimposing the lower–middle tropospheric velocity field over (a) relative humidity and (b) the 2D hydrometeor mass density σ_c. The velocity and relative humidity fields are averaged between $z = 2.3$ and 7.7 km, and σ_c is obtained from an integral of the 3D hydrometeor mass density over the same interval. Figures 8c-h are various components of the z-averaged (between 2.3 and 7.7 km) relative humidity budget explained below.

The relative humidity is given by the familiar formula $\mathcal{H} \equiv e/e_s$, in which e is the vapor pressure and e_s is the saturation vapor pressure. Here, e_s is calculated with respect to liquid-water or ice if the absolute temperature T is above or below $T_0 \equiv 273.15$ K, respectively. The Eulerian time derivative of $\mathcal{H}$ may be decomposed as follows:

$$\frac{\partial \mathcal{H}}{\partial t} = -\mathbf{v} \cdot \nabla \mathcal{H} + \left[\left(\frac{c_{pd}}{R_d \Pi} - \frac{\theta}{e_s} \frac{de_s}{dT} \right) \frac{D\Pi}{Dt} - \frac{\Pi}{e_s} \frac{de_s}{dT} \frac{D\theta}{Dt} + \frac{\epsilon}{q_v(\epsilon + q_v)} \frac{Dq_v}{Dt} \right] \mathcal{H}, \qquad (4)$$

in which $\mathbf{v}$ is the 3D velocity field, ∇ is the 3D spatial gradient operator, $D/Dt \equiv \partial/\partial t + \mathbf{v} \cdot \nabla$ is the material derivative, q_v is the water vapor mixing ratio, $\theta \equiv T/\Pi$ is the potential temperature, $\Pi \equiv (p/p_0)^{R_d/c_{pd}}$ is the Exner function of pressure p normalized to $p_0 \equiv 10^5$ Pa, $\epsilon \equiv R_d/R_v$, R_d (R_v) is the gas constant of dry air (water vapor), and c_{pd} is the isobaric specific heat of dry air. The temperature derivative of e_s is given by the approximate Clausius-Clapeyron relation $de_s/dT = L_{vs} e_s / R_v T^2$, in which L_{vs} is the latent heat of vaporization (L_v) or sublimation (L_s) if $T > T_0$ or $T < T_0$, respectively. The first term on the right-hand side of Eq. (4) is associated with 3D advection. The remaining terms from left to right are attributable to changes of pressure, potential temperature and water vapor mass within a moving fluid parcel.[10]

The $\mathcal{H}$-budget indicates that diabatic moist processes have a measurable impact in the main downdraft region (left of the tilt vector) that contains lower–middle tropospheric air moving toward uptilt locations extending from the center to the periphery of the surface vortex core. Predominantly positive budget contributions from the vapor and potential temperature terms in the downdraft region (Figs. 8d and 8e) are believed to largely stem from endothermic phase changes of water substance, such as evaporation of cloud droplets or rain (inferred to be present from Fig 8b). However, there is a greater negative contribution from the pressure term (Fig. 8c), whose z-t average presumably contains contributions from

[10]The sum of the vapor and potential temperature terms would exactly cancel the pressure term for a saturated cloudy air parcel governed by reversible thermodynamics, in which water substance is conserved and changes phase instantaneously. Otherwise, $\mathcal{H}$ would not remain equal to unity along the saturated parcel trajectory. By contrast, the vapor (potential temperature) term is zero (practically zero) in unsaturated air undergoing reversible adiabatic displacements.

the subsidence of unsaturated air parcels minimally affected by transiting hydrometeors or the turbulent influx of suspended condensate. The net negative forcing (Fig. 8f) is enough to offset most of the positive advective tendency coinciding with a negative downwind gradient of $\mathcal{H}$ (Fig. 8g), as demonstrated by Fig. 8h. Note that the advective tendency is here dominated by its horizontal component (compare Fig. 9a to 9b).

The preceding analysis supports the notion that subsidence can be as effective as the direct intrusion of dry environmental air (which seems largely precluded by the streamlines in Fig. 8a) in maintaining the deficiency of lower–middle tropospheric $\mathcal{H}$ over the central and uptilt regions of the inner core. Evidence for the potential importance of subsidence in this respect can also be found in a number of recent studies of real-world and realistically simulated tropical cyclones possessing appreciable tilt (e.g., DB12; Z16; NRR17; AZZ20).

Whereas the central and uptilt deficits of lower–middle tropospheric relative humidity may be of primary interest, the maintenance of enhanced $\mathcal{H}$ in the vicinity of downtilt convection merits brief consideration before moving on. Figure 8h demonstrates that the net positive forcing of $\mathcal{H}$ in the updraft region (Fig. 8f) effectively counterbalances the negative advective tendency (Fig. 8g). The net positive forcing of $\mathcal{H}$ results from the positive pressure term (Fig. 8c) overcompensating for the negative vapor and potential temperature terms (Figs. 8d and 8e). One might reasonably suppose that such overcompensation in the z-t mean is partly due to positive contributions to the pressure term from unsaturated updrafts. One might also suppose that the overcompensation is partly due to some amount of evaporation or sublimation of detrained or falling condensate, and melting of icy hydrometeors. The positive forcing of $\mathcal{H}$ associated with the aforementioned microphysical processes will lessen the net negative vapor and potential temperature terms that are presumably dominated by contributions from condensation, deposition and (in the latter case) freezing within cloudy updrafts. It is notable that the positive forcing of $\mathcal{H}$ due to evaporation, condensation and melting (Fig. 9c) is actually comparable to the net positive total forcing (Fig. 8f) in the updraft region.

5.b LCAPE

Of course, lower–middle tropospheric $\mathcal{H}$ is not the only thermodynamic factor regulating deep convection. The middle column of Fig. 7 shows the distributions of "lower tropospheric" convective available potential energy, defined by

$$\text{LCAPE} \equiv \int_0^{z_{600}} dz \; g \frac{\theta_{v,\text{prcl}} - \theta_v}{\theta_v}, \tag{5}$$

in which z_{600} is the local height of the 600-hPa pressure isosurface, g is the gravitational acceleration near the surface of the earth, θ_v is the virtual potential temperature of the local atmospheric sounding, $\theta_{v,\text{prcl}}$ is the virtual potential temperature of a local 500-m "mixed-layer" parcel undergoing undiluted pseudoadiabatic ascent, and the integrand as a whole is the parcel buoyancy.[11] Note that both positive and negative buoyancy contributions are included in the integral, so that LCAPE is not always positive. For all SSTs, small (and even negative) values of LCAPE are seen to cover much of the inner core of the surface vortex, including the most central region. Such conditions presumably hinder the local invigoration of deep convection should it be attempted by some forcing mechanism. More favorable conditions of relatively high LCAPE are generally seen in the vicinity of downtilt convection.

The small values of inner-core LCAPE found away from downtilt convection are readily understood from the regional vertical profiles of the (pseudoadiabatic) entropy s^p and saturation entropy s^p_s. Here we use the approximation for s^p in Bryan [2008, Eq. (11)] assuming liquid-only condensate. The selected profiles appearing in the bottom row of Fig. 10 correspond to soundings averaged over 6 hours (starting from $t = t_s$) and within 35-km radii of the white diamonds in the middle column of Fig. 7. Inversions are seen to counter the initial decay of saturation entropy with increasing altitude from the sea surface, resulting in values of s^p_s that exceed or nearly equal the nominal mixed-layer s^p over a sizable fraction of the lower–middle troposphere. Such a state of affairs is consistent with mixed-layer parcels

[11] The parcel buoyancy is calculated as in the *getcape* subroutine included in the CM1 software package.

having small or (over certain intervals) negative buoyancy at altitudes relevant to the LCAPE integral. The foregoing saturation entropy profiles stand in sharp contrast to those found in the vicinity of downtilt convection, where inversions are absent and the values of s_s^p are considerably reduced in the lower–middle troposphere (Fig. 10, top row).

High saturation entropy in the lower–middle troposphere found away from downtilt convection in the inner core coincides with relatively warm air, or equivalently a regional lowering of θ-surfaces (Fig. 11). By contrast, low saturation entropy in the vicinity of the downtilt convection zone coincides with cooler air and elevated θ-surfaces. Such a configuration is at least qualitatively consistent with an atmosphere adjusted to nonlinear balance within a misaligned vortex (see DeMaria 1996). The deviations of the pressure and virtual potential temperature fields (from domain-averaged values) that are quantitatively consistent with nonlinear balance, given the vertical vorticity distribution ($\zeta \equiv \hat{\mathbf{z}} \cdot \nabla \times \mathbf{v}$) of a tropical cyclone, are readily obtained by solving Eqs. (C3) and (C4) of SM20. The corresponding saturation entropy profiles above the boundary layer are shown by the solid grey curves in Fig. 10. They are seen to agree reasonably well with the directly measured (solid black) profiles.

Near-surface moist-entropy deficits do not appear to have a role comparable to that of relatively warm air in the lower part of the troposphere above the boundary layer in causing relatively low values of LCAPE over much of the inner core. The right column of Fig. 7 shows the distributions of a conventional measure of the near-surface moist entropy— the boundary layer equivalent potential temperature θ_{eb} calculated as in Emanuel [1994, Eq. (4.5.11)]. The values of θ_{eb} in the T26 and T30 tropical cyclones are actually peaked near the centers of the surface vortices (Figs. 7c and 7i), where LCAPE is depressed. Such high entropy reservoirs, built up where deep convection is hindered by conditions aloft, are notably reminiscent of that described by Dolling and Barnes (DB12) in their study of tropical storm Humberto (2001). The T28 system differs in that much of its inner region has lower θ_{eb} than that

which is found in the principal air mass entering the downtilt convection zone.[12] However, the deficits of θ_{eb} are no more than 2 K below the core maximum, and do not seem to shape the distribution of LCAPE (compare Fig. 7e to 7f).

The swath of relatively low-entropy air in the boundary layer of the T28 tropical cyclone appears to result from the infusion of low-entropy downdrafts (not shown) in the vicinity of downtilt convection and the associated downwind stratiform precipitation. Though apparently not spreading as far toward the surface center of the tropical cyclone, similar swaths of relatively low-entropy air near and downwind of the convection zone exist in the T26 and T30 systems. While this low-entropy air may not have an obvious role in preventing deep convection at small radii, it could still infiltrate and weaken convective updrafts upon completing a recirculation cycle. The amount of low-entropy air that reaches the convective updrafts cannot be firmly ascertained without a trajectory analysis (cf. RDT18; A21a; Chen et al. 2021), but some insight on its potential impact is readily obtained by considering the time scale for its recovery under the action of the surface enthalpy fluxes[13] depicted in the right column of Fig. 7. The time scale for surface enthalpy fluxes to raise θ_{eb} to the surface saturation level without impediments can be estimated by $\tau_s \sim h_b/C_e v$, in which h_b is the characteristic depth ($\sim$ 1 km) of the boundary layer. The velocity-independent ratio of τ_s to the circulation period $\tau_r \sim 2\pi r/v$ increases from 0.9 to 1.3 to 2.7 as r decreases from 150 to 100 to 50 km. Therefore, the negative impact of downdraft-adulterated air on the intensity of downtilt convection may not be too severe when recirculation occurs at a radius beyond approximately 100 km. Moreover, the streamlines suggest that much of the air mass entering the convection zone in the boundary layer derives not from regions of adulteration in the core, but from elsewhere in the outer vortex. Such would seem consistent with convection that is mechanically supported by the underlying frictional inflow (see appendix A).

[12]The absence of a (relatively) high entropy reservoir near the surface center is believed to be a result of chance, as opposed to being a general characteristic of tilted tropical storms over SSTs of 28 ^{o}C; such reservoirs under depressions of LCAPE are seen in other tropical storms belonging to group T28.

[13]The surface enthalpy flux F_k is calculated here with the conventional approximation in Zhang et al. (2008). The kinematic surface flux of equivalent potential temperature is approximately given by $F_k/\rho c_{pd}$, in which ρ denotes density (e.g., De Ridder 1997).

6. Transition from Slow to Fast Intensification

In our simulations, a major boost of the intensification rate generally entails significant changes to the previously described structure of a tropical cyclone (section 5). The following aims to identify the conditions required for a transition to fast spinup for a given SST. The transition point will be defined so as to occur when the intensification rate begins to sharply grow after maintaining a sufficiently small value over the preceding 20 hours. Bear in mind that this does not necessarily correspond to the onset of rapid intensification (RI), which by its conventional definition occurs when the maximum sustained surface wind speed begins to grow at least 15.4 m s^{-1} ($\pm$ a few m s^{-1}) over 24 hours (Kaplan and DeMaria 2003; Kaplan et al. 2010). Conventional RI may occur after the transition, but is not explicitly required.

6.a The Transition Time

The transition time t_* is identified herein with an ad hoc but objective method that is invariant with the SST and proves to be adequate for the simulations under present consideration. To begin with, the following conditions must be satisfied at t_*: (i) $v_m(t) > v_m(t_*)$ for all $t > t_*$ with 2-h smoothing applied to v_m, (ii) $a_m^- < a_o$, and (iii) $a_m^+ \geq \max(a_o, \alpha a_m^-)$. The variable $a_m^\pm$ appearing in (ii) and (iii) denotes the average of dv_m/dt between t_* and $t_* \pm \delta t_*$. The parameters are tuned to $\alpha = 3.5$, $a_o = 3.0 \times 10^{-5}$ m s^{-2}, and $\delta t_* = 20$ h. An additional measure is taken to overlook any early jump of dv_m/dt that is subsequently nullified, and followed by a long episode of slow intensification. A number of systems are excluded from the forthcoming analysis, because they do not have transitions during the HFP that strictly satisfy the preceding identification criteria. The systems kept include 50% of group T26, 50% of group T28, and 25% of group T30. The small percentage from group T30 results from only the largest initial tilts giving rise to extended periods of sufficiently slow spinup over the warmest ocean.

Figure 12a is a scatter plot of τ_* versus $\tau_{\rm hf}$, in which τ_* denotes t_* minus the start time

of the HFP. The ratio $\tau_*/\tau_{\rm hf}$ is found to equal 0.74 ± 0.07 over the full range of systems retained for analysis.[14] Figures 12b and 12c show v_m and dv_m/dt against $t - t_*$ for the same systems. In general, the transition times seem to adequately capture the moments when the acceleration *begins* to jump to a higher level that is subsequently maintained as the tropical cyclone becomes a hurricane.

6.b Alignment and Axisymmetrization at the Time of Transition

First and foremost, we should verify expectations based on section 4 and a number of complementary studies addressing the onset of RI in systems with moderate shear (e.g., Z16; Munsell et al. 2017; Miyamoto and Nolan 2018; RDT18; AZZ20) that the transition to fast spinup generally occurs after substantial reduction of tilt. Figure 13a depicts the evolving statistics of the tilt magnitude during a 2-day time interval centered at t_*. The left, middle and right panels respectively show data averaged over the intervals $-24 \leq t - t_* \leq -12$, $-6 \leq t - t_* \leq 6$ and $12 \leq t - t_* \leq 24$, in which the end-points are given in hours. In each panel, the data are segregated into three columns according to the SST. The colored box in a given column extends vertically from the first to third quartile of the data associated with the pertinent SST. The dashed horizontal line within a box indicates the location of the median tilt magnitude. The columns also contain scatter plots of the SST-segregated data sets. The data points in each scatter plot are arranged from left to right in order of increasing values of the initial tilt magnitude ($tilt_0$) of the simulation. Rulers for $tilt_0$ are shown on the top of each panel. Regardless of the SST, the median tilt magnitude drops significantly from the pre-transitional time period to the transition time. The trend continues as fast spinup progresses. Figure 13b depicts the evolving statistics of the precipitation asymmetry [Eq. (3) with $a = 200$ km]. The plotting conventions are as in Fig. 13a. The results for P_{asym} are similar to those obtained for the tilt magnitude, because the two variables are dynamically correlated in the tropical cyclones under present consideration.

[14] Here and elsewhere, $a \pm b$ denotes the mean (a) $\pm$ one standard deviation (b) of a data set.

The preceding analysis supports the notion that a sufficient reduction of the tilt magnitude occurring simultaneously with a reduction of asymmetry in precipitating convection has an important role in enabling a transition to fast spinup. Overall, the coupled values of the tilt magnitude and P_{asym} that mark the transition for group T26 are appreciably smaller than their counterparts for groups T28 and T30 (see the middle panels of Figs. 13a and 13b). A fairly similar result is found for the transitional ratio of the tilt magnitude normalized to r_m, which is 0.31 ± 0.12 for group T26, 0.54 ± 0.21 for group T28, and 0.74 ± 0.24 for group T30. Alvey and coauthors (AZZ20) notably reported that a comparable variable having a value below 0.75 was generally needed for RI in an ensemble of simulations of tropical cyclone Edouard (2014) over an SST of 28-30 ^{o}C. As an aside, it is worth remarking that the reductions of tilt and precipitation asymmetry seen here do not coincide with a transition to an approximate state of slantwise convective neutrality that is sometimes assumed in analytical intensification theories (see appendix B).

In contrast to the behavior of *tilt* and P_{asym}, the magnitude of r_m tends not to appreciably decline during the day preceding the transition time t_* (Fig. 13c). Contraction of the inner core of the surface vortex is generally more evident in the day that follows, as the intensification of v_m accelerates. Unshown time series demonstrate that the decline of r_m after t_* is normally sharper in group T30 than in groups T28 and T26, although some members of group T28 shortly exhibit abrupt contraction. In general, the reduction of r_m coincides with a similar reduction of the precipitation radius r_p. Quantitatively, the ratio of r_m (r_p) at the end of the HFP over its value found during the transitional time period is 0.37 ± 0.16 (0.42 ± 0.14). The preceding statistics are for the ensemble of all analyzed systems; the T26-ratios are mostly on the upper ends of the distributions. Note further that the post-transitional value of r_p/r_m tends not to stray too far above unity over time.

6.c Moist-Thermodynamic Conditions at the Time of Transition

In the experiments under present consideration, the reduction of tilt coincides with modifi-

cations of the moist-thermodynamic conditions of the vortex core that in the aggregate are believed to facilitate the faster spinup that ensues. These modifications are best explained by way of an illustrative example. Consider the tropical cyclone in simulation T28-HRA. Figures 7d-f depict the state of the system 14-20 hours prior to t_*. Figures 14a-c show the same fields averaged over a 6-h time window centered at t_*. The latter transitional state is clearly distinguished by having a smaller misalignment of middle and lower tropospheric circulations. In addition, the transitional state has lost the strong downtilt bias seen earlier in the distribution of deep convection. The previously small values of LCAPE uptilt and near the center of the surface vortex have also been eliminated. Furthermore, there are substantial enhancements of lower–middle tropospheric relative humidity and boundary layer equivalent potential temperature over much of the inner core.

Figure 14d compares the central vertical distributions of entropy and saturation entropy during the foregoing 6-h pre-transitional and transitional time periods of the tropical cyclone evolution. The distributions are averaged within a 35-km radius of the surface vortex center. In contrast to the pre-transitional state, the transitional state exhibits monotonic decay of s_s^p with increasing z in the lower–middle troposphere, and enhanced s^p at essentially all altitudes up to the tropopause. The entropic changes coincide with lower–middle tropospheric cooling above the boundary layer, and a relatively deep augmentation of q_v (Fig. 14e). The transitional state also exhibits warming in the upper troposphere. Both the upper warming and lower cooling are consistent with the maintenance of nonlinear balance during pre-transitional alignment.[15] The solid curve in Fig. 14f shows the transitional distribution of the azimuthally averaged deep-layer CAPE[16] minus that of the pre-transitional system in a surface-vortex centered coordinate system. A measurable boost of deep-layer CAPE is found inward of r_m.

[15]The author has verified the existence of a similar pattern in the vertical profile of the central temperature difference between balanced vortices having the same ζ-distributions as the actual transitional and pre-transitional vortices.

[16]The deep-layer CAPE is defined here as the positive contribution to the vertical buoyancy integral of a 500-m mixed-layer parcel ascending pseudoadiabatically to the *highest* tropospheric equilibrium level. The highest equilibrium level is usually near the tropopause and may exceed the lowest equilibrium level. Thus, the deep-layer CAPE ignores potential termination of ascent in the lower troposphere.

At the radius of maximum gain, the thermal velocity ($\sqrt{2\text{CAPE}}$) increases from 54.6 to 63.3 m s^{-1}. Perhaps more significant is the dashed curve reflecting a large fractional boost of azimuthally averaged LCAPE (from 54 to 254 J kg^{-1} at $r = 0$) connected to the increase of T and q_v in the boundary layer along with cooling in the lower part of the free troposphere. Considering this in combination with the 5-15% enhancement of lower–middle tropospheric relative humidity that is shown by the dash-dotted curve, the inner core of the transitional tropical cyclone seems appreciably more conducive to deep convection. In a general sense, the foregoing improvement of inner-core moist-thermodynamic favorability for deep convection attending the reduction of tilt and leading to faster intensification is not unlike that seen in typical studies of real and realistically simulated tropical cyclones that transition to RI (e.g., Z16; AZZ20). The extent to which differences in details at the transition time— resulting from the environmental shear-flow commonly present in a real system —might fundamentally alter the mode of intensification that follows is currently unknown, and will be deferred to future study.

The forthcoming analysis will confirm that the key inner core enhancements of relative humidity and LCAPE seen above to precede fast spinup are common across the broader spectrum of shear-free systems under present consideration. The analysis will also determine how the moist-thermodynamic aspects of the transition from slow to fast spinup vary *quantitatively* with the SST.

For notational convenience in what follows, let G represent either $\mathcal{H}$, LCAPE, CAPE, the surface enthalpy flux F_k, or the surface precipitation rate P. Here and for the remainder of section 6, $\mathcal{H}$ and CAPE should be understood to represent *lower–middle tropospheric* relative humidity[17] and *deep-layer* CAPE, respectively. Continuing, let G^c denote the areal average of G over a surface vortex centered circular disc of radius r_c. Let G^c_- denote the temporal average of G^c over the pre-transitional time period given by $-24 \leq t - t_* \leq -12$ h, with r_c set equal to a similar temporal average of βr_m. Define G^c_* in a similar way, but with the temporal

[17]Lower–middle tropospheric relative humidity is measured in the following analysis as in section 5 by taking a vertical average between $z = 2.3$ and 7.7 (7.8) km for HR (LR) simulations.

averaging over the transitional time period given by $-6 \leq t - t_* \leq 6$ h. The parameter β is set equal to 1 for $G \in \{\mathcal{H}, \mathrm{LCAPE}, \mathrm{CAPE}\}$ so that the areal averages represent conditions immediately relevant to the invigoration of deep convection inward of r_m. A moderately larger β (1.5) is used for P to incorporate rainfall that extends to the outer proximity of r_m, and for F_k to incorporate the impact of near-surface moist-entropy perturbations that may occur in the area of that rainfall. Figure 15a tabulates the mean values and standard deviations of G^c_- and G^c_* for all pertinent moist-thermodynamic variables in each SST-group. Similar data are shown for the pre-transitional and transitional values of the tilt magnitude ($tilt_-$ and $tilt_*$) whose decay goes hand in hand with the moist-thermodynamic modifications of the tropical cyclone. Figure 15b depicts the SST-segregated distributions of the fractional change of each core-averaged variable between the pre-transitional and transitional time periods, given by the generic formula

$$\delta G^c \equiv \frac{G^c_* - G^c_-}{G^c_-}. \tag{6}$$

The distribution of $\delta tilt \equiv \frac{tilt_* - tilt_-}{tilt_-}$ is also displayed.

Referring to Fig. 15b, all SST groups show appreciable median fractional boosts of $\mathcal{H}^c$ and LCAPE^c over the day leading up to t_*. The boosts of LCAPE^c tend to coincide with modest gains of equivalent potential temperature in the boundary layer, but the two changes are not well correlated,[18] as other factors such as lower–middle tropospheric cooling (Fig. 14e) have substantial impact. The distributions for the fractional changes of CAPE^c differ from those of LCAPE^c in having smaller medians, and in one case (group T26) a negative median. One notable factor that may contribute to a negative change of CAPE is upper tropospheric warming (Fig. 14e). The core enthalpy flux F^c_k tends to decline prior to t_* by increasing fractional amounts with increasing SST. Such decline indicates a minor reduction of air-sea disequilibrium and/or surface wind speed immediately preceding fast spinup. The median

[18] With θ^c_{eb-} (θ^c_{eb*}) denoting the pre-transitional (transitional) average of θ_{eb} within a disc of radius r_m, $\theta^c_{eb*} - \theta^c_{eb-} = 0.48 \pm 0.31$ K for group T26, 1.15 ± 0.79 K for group T28, and 0.53 ± 1.55 K for group T30. The correlation coefficients between $\mathrm{LCAPE}^c_* - \mathrm{LCAPE}^c_-$ and $\theta^c_{eb*} - \theta^c_{eb-}$ are -0.32 for group T26, -0.29 for group T28, and 0.57 for group T30.

fractional change of the core precipitation rate is non-negligible, but inconsistent in switching from a positive to negative value with increasing SST. Relatively large boosts of P^c are not seen until after the transitional time period (not shown).

Whereas some of the moist-thermodynamic changes coinciding with alignment over the day before t_* may be incidental for a transition to fast spinup, others are presumably essential. It would be difficult to argue that the reduction of the surface enthalpy flux should directly promote a transition. On the other hand, the enhancements of $\mathcal{H}^c$ and moist instability–reflected primarily in the growth of LCAPE^c –seem beneficial. Note that the mean transitional value of $\mathcal{H}^c$ decreases from 91 to 81 percent as the SST increases from 26 to 30 ^{o}C (Fig. 15a). The drop is statistically significant (from group T26 to T28 or T30, but not from T28 to T30) as determined by a p-value less than 0.05 in Welch's t-test. Greater mean values of F_k^c and CAPE^c over warmer oceans (Fig. 15a) may help compensate for the less humid lower–middle troposphere and greater tilt magnitude in the recipe for a transition to fast spinup. Their monotonic growth with the SST may also help explain why the wind speed accelerations increase with the SST on average shortly after the transition (Fig. 12c). Interestingly, the mean transitional value of LCAPE^c does not significantly vary with the SST (Fig. 15a).

6.d Comparison to Moist-Thermodynamic Preconditioning for Fast Spinup in Symmetrized Systems

Section 4 showed that removing a large tilt while leaving the symmetric part of the vortex unchanged can hasten the formation of a hurricane. The following demonstrates that the shorter HFP is generally linked to faster achievement of the moist-thermodynamic conditions seen above to signal (alongside reduced tilt) an imminent transition to fast spinup. When such conditions initially exist, symmetrization will be found to prevent their early breakdown.

Figure 16 shows time series of various tropical cyclone parameters for the three LR simulations considered in section 4 from (left to right) groups T30, T28 and T26. These parameters include (top to bottom) v_m, LCAPE^c, $\mathcal{H}^c$ and r_m. The values of LCAPE^c and $\mathcal{H}^c$ are

calculated with $r_c = r_m(t)$. Each plot contains results from the unmodified tilted (principal) system and two restarts in which the tropical cyclones are initially symmetrized as explained in section 4. The first restart (denoted T$*$R1, in which $*$ is the SST) is at the beginning of the HFP, whereas the second (T$*$R2) is in the middle of the HFP. The tilt magnitudes of the principal systems (grey curves) are shown for reference in the bottom panels.

The principal T30 simulation and T30R1 begin the HFP with LCAPE^c and $\mathcal{H}^c$ having values near the high ends of the transitional levels found in section 6c. In T30R1, LCAPE^c and $\mathcal{H}^c$ promptly increase (Figs. 16b and 16c), and the tropical cyclone consistently moves into a stage of fast spinup (Fig. 16a). Such growth of the intensification rate appears to be hindered in the principal simulation by growth of the tilt magnitude (Fig. 16d) and attendant declines of moist-thermodynamic parameters to subtransitional levels (Figs. 16b and 16c). T30R2 begins before LCAPE^c and $\mathcal{H}^c$ are able to recover. Evidently, symmetrization expedites the recovery and coinciding transition to fast spinup. As in the principal simulation, a sharp reduction of r_m occurs in T30R2 when the fast mode of intensification takes over (Fig. 16d). Note that late drops of LCAPE^c and $\mathcal{H}^c$ appearing in Figs. 16b and 16c are presumably associated with the development of the eye of a strengthening hurricane.

The principal T28 simulation begins the HFP having LCAPE^c within and $\mathcal{H}^c$ below the statistical spreads of their transitional levels. Both parameters promptly decay and tend to stay below their mean transitional levels for several days (Figs. 16f and 16g), while the tilt magnitude remains above $tilt_* \approx 44$ km (Fig. 16h). Subsequent growth of LCAPE^c and $\mathcal{H}^c$ leads to appreciable acceleration of intensification (Figs. 16e-g), but the change is too gradual for the identification of a transition point by the rules of section 6a. The symmetrized tropical cyclones (in T28R1 and T28R2) also begin in states having LCAPE^c within and $\mathcal{H}^c$ below the statistical spreads of their transitional levels. However, both parameters increase rapidly, and faster spinup occurs soon after $\mathcal{H}^c$ joins LCAPE^c in rising to where a transition can be expected (Figs. 16e-g). The T26 simulations (Figs. 16i-l) do not require lengthy discussion, as they are qualitatively similar to their T28 counterparts.

It has been shown that our symmetrized tropical cyclones expeditiously begin accelerated intensification in conjunction with LCAPE^c and $\mathcal{H}^c$ quickly acquiring or maintaining values that equal or exceed those within one standard deviation of the statistical means of LCAPE^c_* and $\mathcal{H}^c_*$. The preceding result is consistent with the proposition that the moist-thermodynamic changes coinciding with reduced tilt in our simulations, which facilitate deep convection inward of r_m, are essential to enabling the onset of fast spinup. The mechanisms controlling the time scale of the alignment process that brings forth a state conducive to fast spinup were addressed in SM20 for systems in group T28. While the present study will not delve further into the intricate mechanics of alignment, those interested may consult appendix C for a brief discussion of how the alignment rate varies with the SST.

7. Summary and Conclusions

A cloud resolving numerical model has been used to examine how depression-strength tilted tropical cyclones evolve into hurricanes over oceans having a range of SSTs. The simulations analyzed herein were distinguished from those of earlier studies (barring SM20) in focusing on the evolution that occurs when environmental vertical wind shear— which may have created the initial tilt —is reduced to a negligible level. The length τ_{hf} of the hurricane formation period (HFP) at any SST was shown to exhibit approximate linear growth with either the initial tilt magnitude (above a threshold) or the positively correlated time average of the radius of maximum wind speed r_m. Moreover, decreasing the SST led to superlinear growth of τ_{hf}. For a given time average of r_m exceeding approximately 40 km, the growth of τ_{hf} upon cooling the ocean surface from 30 to 28 ^{o}C was an order of magnitude smaller than the growth upon further cooling to 26 ^{o}C. The disproportionately smaller growth of τ_{hf} over the first two-degree drop coincided with a disproportionately smaller (negligible by the measure in Fig. 2b) reduction of the precipitation rate integrated over the core of the surface vortex.

The evolution of a strongly tilted tropical cyclone was often found to have a prolonged phase of slow (or neutral) intensification followed by fast spinup. The slow phase of intensi-

fication persists while the tropical cyclone maintains a state of substantial vertical misalignment with deep convection concentrated far downtilt from the center of the surface vortex. There was some concern that an early expansion of the inner core that occurs in response to the initial misalignment (SM20) could have set the tropical cyclone on course for slow intensification regardless of whether the structural asymmetry is retained. The preceding concern was allayed upon finding considerably faster development in a number of restarts beginning with the tilt-related asymmetry removed after the inner core expands.

The off-center asymmetric organization of convection associated with sustained tilt and slow spinup was analyzed for selected tropical storms at several SSTs. While details may differ to some extent, results were qualitatively similar at all SSTs, and in many respects resembled those reported in earlier studies of real and realistically simulated tropical cyclones that are tilted by moderate environmental vertical wind shear (as explained in section 5). The analyses suggested that a combination of reduced lower–middle tropospheric relative humidity $\mathcal{H}$ and lower tropospheric convective available potential energy (LCAPE) discourages the invigoration of deep cumulus convection near the surface vortex center and uptilt. By contrast, high values of $\mathcal{H}$ and LCAPE were found to facilitate deep convection in a region of boundary layer convergence located off-center and downtilt. Examination of individual tendency terms for lower–middle tropospheric $\mathcal{H}$— in one particular case chosen for detailed analysis —suggested that its low values uptilt and near the surface vortex center are primarily maintained by mesoscale subsidence to the left of the tilt vector. Low values of LCAPE over the bulk of the inner core outside the vicinity of downtilt convection seemed largely connected to relatively warm air in the lower part of the troposphere above the boundary layer. Such warming was shown to be consistent with that expected for a misaligned tropical cyclone in a state of nonlinear balance in the free atmosphere.

The transition to fast spinup occurs after the tilt magnitude becomes sufficiently small through an alignment process discussed in SM20 and appendix C. This geometrical change was shown to coincide with enhancements of lower–middle tropospheric $\mathcal{H}$ and LCAPE

within a surface vortex centered disc of radius r_m. The moist-thermodynamic changes attending tilt-reduction seem crucial for initiating a fast, relatively symmetric intensification process that involves simultaneous contraction of r_m and the characteristic radius of deep convection. The mean transitional value of LCAPE was found to have no statistically significant variation with the SST. By contrast, the mean transitional values of the tilt magnitude and lower–middle tropospheric $\mathcal{H}$ over relatively warm oceans (having SSTs of 28 or 30 ^{o}C) were respectively higher and lower than their counterparts over the coolest ocean (having an SST of 26 ^{o}C). It is provisionally proposed that greater magnitudes of the surface enthalpy flux F_k and deep-layer CAPE in the cores of tropical cyclones over warmer oceans help compensate for the less complete alignment and core humidification. The monotonic growth of the mean transitional values of F_k and deep-layer CAPE with the SST may furthermore contribute to the positive correlation seen between the SST and the immediate post-transitional wind speed acceleration.

Two notable elements of a natural system— radiative forcing and environmental vertical wind shear —were left out of the simulations considered for this study. Including a realistic parameterization of radiative transfer in the model is expected to accelerate hurricane formation, but the detailed consequences on the foregoing results are presently unknown. There presumably exists a parameter regime of sufficiently weak shear in which there is no radical change to the relationship between the tilt magnitude and the moist-thermodynamic structure of the tropical cyclone seen here under quiescent environmental conditions. In the same parameter regime, there would be no obvious reason to expect a major change to the coupled kinematic and moist-thermodynamic conditions that enable a transition from slow to fast spinup, or to the alignment process that goes hand in hand with creating those conditions (SM20). Determination of the precise level of shear at which major deviations begin to emerge has been left for future study.

Acknowledgments and Data Statement: The author gratefully acknowledges the thorough and constructive feedback of several anonymous reviewers. The author also thanks Dr. George

Bryan of the National Center for Atmospheric Research (NCAR) for providing the cloud-resolving model (CM1) that was used to simulate the development of the tilted tropical cyclones considered herein. Finally, the author thanks Peter Rosenthal for running and conducting preliminary analyses on numerous simulations used for this study during a summer internship at NorthWest Research Associates. All work for this paper including that related to the aforementioned internship was supported by the National Science Foundation under Grant AGS-1743854. The computational resources required to conduct the HR simulations were provided by NCAR's Computational and Information Systems Laboratory (doi:10.5065/D6RX99HX). Archived simulation output and configuration files are presently maintained by the author and can be made available upon request to any researcher with a legitimate need.

Appendix A

The Role of Surface Friction in Maintaining Deep Convection Downtilt

Figure A1 provides some verification of the reasonable presumption that forcing of updrafts by frictional convergence in the boundary layer has an important role in maintaining the vigor of deep convection that occurs downtilt during the HFP. Figures A1a and A1b show two sequential plots of the 6-h accumulated precipitation and the 6-h time-averaged upper-tropospheric vertical velocity field in simulation T28-HRA. The sequence begins at $t = t_s - \delta t$, in which t_s is the start time of the averaging window in Figs. 7d-f, and $\delta t = 6$ h. Figures A1d and A1e show similar plots for a restart of the simulation at time $t_s - \delta t$, with the surface drag coefficient C_d homogenized and reduced by two orders of magnitude so as to equal 2.5×10^{-5}. Evidently, the reduction of C_d causes convection to rapidly dissipate and virtually vanish within 12 hours. Such dissipation coincides with pronounced decay of the inward boundary layer mass-flux seen in a complementary Hovmöller plot of $r\bar{u}$ averaged over the interval $0 \leq z \leq 1$ km (Fig. A1f). No such decay is found in the control run (Fig. A1c).

The preceding result should not be overgeneralized, but raises questions on the impor-

tance of certain hypothetical boosters for deep convection downtilt. One possible booster is adiabatic upgliding to the right of the tilt vector, which could lift initially unsaturated air to its level of free convection downtilt. It is unclear why convection supported by such a mechanism would so rapidly break down upon the reduction of surface drag. Another booster could be a robust cold pool downstream of convection, but there is no evidence of this scenario appreciably compensating for the removal of frictional convergence in the tropical storm considered above. The extent to which asymmetries in Ekman-like pumping may help give rise to a downtilt bias for deep convection near r_m has not been investigated for the systems at hand. However, a concentration of deep convection downtilt would seem to be the most likely outcome of the broader frictional inflow, given the less conducive moist-thermodynamic conditions existing elsewhere.

Appendix B

Distinction Between the Transition to Fast Spinup and the Transition to SCN

There has been a longstanding interest in tropical cyclone intensification theories that assume an azimuthally averaged state in which angular momentum contours arising from the vicinity of maximum wind speed are congruent with saturation entropy contours above the boundary layer (e.g., Emanuel 1997,2012; Peng et al. 2018). Such a condition of slantwise convective neutrality (SCN) and any dependent theory are generally inapplicable to cloud resolving simulations of early development. However, there is some computational evidence that SCN may be a reasonable approximation after an axisymmetric tropical cyclone intensifies beyond a transition point along its path toward equilibrium, where SCN in the eyewall is ideally exact (e.g., Peng et al. 2018).

To be clear, the transition to fast spinup in the present simulations entails a reduction of asymmetry, but generally does not coincide with a transition to SCN in an emergent eyewall. Figure B1 depicts the azimuthal-mean states of selected T26, T28 and T30 tropical cyclones, time averaged over 6-h intervals centered at (top row) t_* and (bottom row) t_* plus

21 hours. In all cases, the angular momentum and saturation entropy contours are incongruent throughout the vortex core, especially in the lower troposphere (cf. Schecter 2011,2016).

Appendix C

Alignment and Precession

Given that sufficiently large tilt magnitudes are correlated to unfavorable moist-thermodynamic conditions for intensification in our simulations, the time scale for the onset of fast spinup is linked to the time scale of vertical alignment. The time scale of alignment depends on the specific mechanism, which can be diabatic, adiabatic or more generally some hybrid of the two. Efforts to understand the mechanisms operating in pre-hurricane vortices, which partly involves elucidating the roles played by different facets of moist-convection, are ongoing (e.g., Nguyen and Molinari 2015; Chen et al. 2018; RDT18; SM20; AZZ20; Rogers et al. 2020). SM20 began to examine the alignment process for the HR T28 simulations of the present study and identified 3 distinct stages. The first stage is characterized by a rapid decay of the tilt magnitude that involves the swift diabatically driven migration of the surface center toward deep convection downtilt, and in some cases the reformation of the middle tropospheric vorticity core closer to the surface center. The second stage is characterized by transient growth of the tilt magnitude, and is most pronounced in tropical cyclones initialized with the largest misalignments. In one system selected for detailed analysis (T28-HRA of this paper), the transient growth seemed partly caused by the emergence of a peripheral patch of anticyclonic vorticity (in the middle troposphere) that nudges the principal part of the midlevel cyclonic vorticity distribution away from the surface center; diabatic processes appeared to modulate the drift. The third stage of alignment identified in SM20 operates during much of the HFP, and typically involves gradual decay of the tilt magnitude. In the aforementioned case study, the gradual decay was driven by a complex interplay between diabatic forcing and adiabatic vortex dynamics, and failed to occur when moisture was removed from the simulation. Bear in mind that the third stage of alignment is not always purely gradual or monotonic, in that it sometimes contains notable secondary episodes of

rapid decay or transient growth of the tilt magnitude.

While providing valuable insights, SM20 did not consider how the alignment process depends on the SST. Figure C1a addresses the foregoing deficiency by showing how the time series of the tilt magnitude varies with the SST for the illustrative subset of simulations with $318 \leq tilt_0 \leq 367$ km and a splitting altitude (see section 2b) of $z_l = 5.25$ km. The narrow range of $tilt_0$ and common value of z_l is to ensure that all included simulations have comparable initial conditions. The thin dark curves in the plot correspond to the group mean values of *tilt*, and the thick semitransparent background curves extend vertically from the minimum to maximum group values of *tilt*. Note that the number of simulations in any particular group can decrease with time, since each time series is terminated at the end of the HFP.

Figure C1a demonstrates (for strongly misaligned systems) that increasing the SST from 26 to 30 ^{o}C intensifies the initial decay of the tilt magnitude and diminishes the subsequent transient growth. Consequently, increasing the SST decreases the tilt magnitude at the end of stage 2 of the alignment process. Moreover, the mechanisms working to align the tropical cyclones during stage 3 appear to be least efficient in the long term over the coolest ocean.

As mentioned in section 1, reducing the environmental vertical wind shear to a negligible level eliminates the potential importance of tilt reorientation to the alignment process. However, precession of the tilt vector can still factor into the time scale for alignment. Before discussing how, let us first examine the nature of precession for the systems considered herein. Figure C1b illustrates the evolution of the tilt angle (φ_{tilt}, measured counterclockwise from the positive x-direction in Fig. 7) for all simulations having well defined transitions to fast spinup before the end of the HFP. The tropical cyclones in all SST groups exhibit a precession frequency ($d\varphi_{tilt}/dt$) of order 10^{-5} s^{-1} in the days leading up to t_*. There is only one outlier from group T26 (dotted blue line) that has an episode of fast precession prior to the official transition time. This episode coincides with a short-lived state of very small tilt and relatively large wind speed acceleration that is disrupted by the restoration of modest tilt, well before v_m can appreciably intensify. The general boost of the precession frequency

in groups T26 and T28 immediately after the onset of fast spinup is also notable, but of questionable significance given the smallness of the tilt magnitude for $t > t_*$.

S20 theorized that the azimuthal propagation of downtilt convection coinciding with precession can either hinder or help the diabatically induced migration of the surface center toward the midlevel center of the tropical cyclone. In theory, the potentially positive influence becomes most evident when the azimuthal velocity of the propagation exceeds a certain threshold that allows lower tropospheric vorticity to very efficiently amplify in the convection zone, thereby causing core reformation. The aforementioned threshold depends on several factors, and most notably decreases with increasing strength of the diabatic forcing that enhances convergence in the downtilt convection zone. For the simulations considered above, the precession leading up to fast spinup has a much smaller angular velocity than the characteristic rotation frequency of the cyclonic circulation ($v_m/r_m \gtrsim 10^{-4}$ s^{-1}). The corresponding slowness of the azimuthal propagation of downtilt convection may have kept the bar too high on the required strength of the diabatic forcing to have seen an irrefutable case of alignment via lower tropospheric core reformation, indicated by an abrupt downtilt jump of $\mathbf{x}_{cs}$. Regarding this point, S20 explicitly verified that the hypothetical condition for core reformation is not satisfied during a representative interval of the slow intensification phase of simulation T28-HRA (appendix A therein).

As a final remark on the subject, a number of theoretical studies preceding S20 suggested that a wave-flow resonance associated with precession might be able to efficiently damp the tilt of a tropical cyclone (e.g., Reasor et al. 2001; Schecter and Montgomery 2003,2007). SM20 considered the potential relevance of resonant damping during the HFP, and provisionally concluded that it should not have substantial impact when precession tends to be as slow as that seen here before the onset of fast spinup.

References

Alland, J.J., B.H. Tang, K.L. Corbosiero, and G.H. Bryan, 2021a: Combined effects of midlevel dry air and vertical wind shear on tropical cyclone development. Part I: Downdraft ventilation. *J. Atmos. Sci.*, **78**, 763-782.

Alland, J.J., B.H. Tang, K.L. Corbosiero, and G.H. Bryan, 2021b: Combined effects of midlevel dry air and vertical wind shear on tropical cyclone development. Part II: Radial ventilation. *J. Atmos. Sci.*, **78**, 783-796.

Alvey III, G.R., E. Zipser, and J. Zawislak, 2020: How does Hurricane Edouard (2014) evolve toward symmetry before rapid intensification? A high-resolution ensemble study. *J. Atmos. Sci.*, **77**, 1329-1351.

Bryan, G.H., and J.M. Fritsch, 2002: A benchmark simulation for moist nonhydrostatic numerical models. *J. Atmos. Sci.*, **130**, 2917-2928.

Bryan, G.H., 2008: On the computation of pseudoadiabatic entropy and equivalent potential temperature. *Mon. Wea. Rev.*, **136**, 5239-5245.

Brown, R.G., and C. Zhang, 1997: Variability of midtropospheric moisture and its effect on cloud-top height distribution during TOGA COARE. *J. Atmos. Sci.*, **54**, 2760-2774.

Carrasco, C.A., C.W. Landsea, and Y.L. Lin, 2014: The influence of tropical cyclone size on its intensification. *Weather and Forecasting*, **29**, 582-590.

Chen, H., and S.G. Gopalakrishnan, 2015: A study on the asymmetric rapid intensification of Hurricane Earl (2010) using the HWRF system. *J. Atmos. Sci.*, **72**, 531-550.

Chen, X., Y. Wang, J. Fang, and M. Xue, 2018: A numerical study on rapid intensification of Typhoon Vicente (2012) in the South China Sea. Part II: Roles of inner-core processes. *J. Atmos. Sci.*, **75**, 235-255.

Chen, X., J.F. Gu, J.A. Zhang, F.D. Marks, R.F. Rogers, and J.J. Cione, 2021: Boundary layer recovery and precipitation symmetrization preceding rapid intensification of tropical cyclones under shear. *J. Atmos. Sci.*, **78**, 1523-1544.

Črnivec, N., R.K. Smith, and G. Kilroy, 2016: Dependence of tropical cyclone intensification rate on sea-surface temperature. *Q. J. R. Meteorol. Soc.*, **142**, 1618-1627.

DeMaria, M., 1996: The effect of vertical shear on tropical cyclone intensity change. *J. Atmos. Sci.*, **53**, 2076-2088.

De Ridder, K., 1997. Land surface processes and the potential for convective precipitation. *J. Geophys. Res.*, **102**, 30085-30090.

Dolling, K. and G.M. Barnes, 2012: Warm-core formation in tropical storm Humberto (2001). *Mon. Wea. Rev.*, **140**, 1177-1190.

Donelan, M.A., B.K. Haus, N. Reul, W.J. Plant, M. Stiassnie, H.C. Graber, O.B. Brown, and E.S. Saltzman, 2004: On the limiting aerodynamic roughness of the ocean in very strong winds. *Geophys. Res. Lett.*, **31**, L18306:1-5.

Drennan, W.M., J.A. Zhang, J.R. French, C. McCormick, and P.G. Black, 2007: Turbulent fluxes in the hurricane boundary layer. Part II: Latent heat flux. *J. Atmos. Sci.*, **64**, 1103-1115.

Dunion, J.P., 2011: Rewriting the climatology of the tropical North Atlantic and Caribbean Sea atmosphere. *J. Climate*, **24**, 893-908.

Emanuel, K.A., 1994. *Atmospheric Convection*, Oxford Univ. Press, New York, 580 pp.

Emanuel, K.A., 1997: Some aspects of hurricane inner-core dynamics and energetics. *J. Atmos. Sci,*, **54**, 1014-1026.

Emanuel, K., 2012: Self-stratification of tropical cyclone outflow. Part II: Implications for storm intensification. *J. Atmos. Sci*, **69**, 988-996.

Fairall, C.W., E.F. Bradley, J.E. Hare, A.A. Grachev, and J.B. Edson, 2003: Bulk parameterization of air-sea fluxes: Updates and verification for the COARE algorithm. *J. Climate*, **16**, 571-591.

Finocchio, P.M., S.J. Majumdar, D.S. Nolan, and M. Iskandarani, 2016: Idealized tropical cyclone responses to the height and depth of environmental vertical wind shear. *Mon. Wea. Rev.*, **144**, 2155-2175.

Gu, J.F., Z.M. Tan, and X. Qiu, 2019. Intensification variability of tropical cyclones in directional shear flows: Vortex tiltconvection coupling. *J. Atmos. Sci*, **76**, 1827-1844.

Hendricks, E.A., M.S. Peng, B. Fu, and T. Li, 2010: Quantifying environmental control on tropical cyclone intensity change. *Mon. Wea. Rev.*, **138**, 3243-3271.

James, R.P., and P.M. Markowski, 2010: A numerical investigation of the effects of dry air aloft on deep convection. *Mon. Wea. Rev.*, **138**, 140-161.

Jones, S.C., 2000: The evolution of vortices in vertical shear. III: Baroclinic vortices. *Quart. J. Roy. Meteor. Soc.*, **126**, 3161-3185.

Kaplan, J., and M. DeMaria, 2003: Large-scale characteristics of rapidly intensifying tropical cyclones in the North Atlantic basin. *Weather and Forecasting*, **18**, 1093-1108.

Kaplan, J., M. DeMaria, and J.A. Knaff, 2010: A revised tropical cyclone rapid intensification index for the Atlantic and eastern north Pacific basins. *Weather and Forecasting*, **25**, 220-241.

Kilroy, G., and R.K. Smith, 2013: A numerical study of rotating convection during tropical cyclogenesis. *Quart. J. Roy. Meteor. Soc.*, **139**, 1255-1269.

Lin, Y., M. Zhao, and M. Zhang, 2015: Tropical cyclone rainfall area controlled by relative sea surface temperature. *Nature Comm.*, **6**, 1-7.

Miyamoto, Y., and T. Takemi, 2015: A triggering mechanism for rapid intensification of tropical cyclones. *J. Atmos. Sci*, **72**, 2666-2681.

Miyamoto, Y., and D.S. Nolan, 2018: Structural changes preceding rapid intensification in tropical cyclones as shown in a large ensemble of idealized simulations. *J. Atmos. Sci*, **75**, 555-569.

Montgomery, M.T., R.K. Smith, 2014: Paradigms for tropical cyclone intensification. *Aust. Meteor. Ocean. Journ.*, **64**, 37-66.

Morrison, H., J.A. Curry, and V.I. Khvorostyanov, 2005: A new double-moment microphysics parameterization for application in cloud and climate models. Part I: Description. *J. Atmos. Sci.*, **62**, 1665-1677.

Morrison, H., G. Thompson, and V. Tatarskii, 2009: Impact of cloud microphysics on the development of trailing stratiform precipitation in a simulated squall line: Comparison of one-and two-moment schemes. *Mon. Wea. Rev.*, **137**, 991-1007.

Munsell, E.B., F. Zhang, J.A. Sippel, S.A. Braun, and Y. Weng, 2017: Dynamics and predictability of the intensification of Hurricane Edouard (2014). *J. Atmos. Sci.*, **74**, 573-595.

Nguyen, L.T., and J. Molinari, 2015: Simulation of the downshear reformation of a tropical cyclone. *J. Atmos. Sci.*, **72**, 4529-4551.

Nguyen, L.T., R.F. Rogers, and P.D. Reasor, 2017: Thermodynamic and kinematic influences on precipitation symmetry in sheared tropical cyclones: Bertha and Cristobal (2014). *Mon. Wea. Rev.*, **145**, 4423-4446.

Nolan, D.S., 2007: What is the trigger for tropical cyclogenesis? *Aust. Met. Mag.*, **56**, 241-266.

Nolan, D.S. and E.D. Rappin, 2008. Increased sensitivity of tropical cyclogenesis to wind shear in higher SST environments. Geophysical research letters, 35(14).

Onderlinde, M.J., and D.S. Nolan, 2016: Tropical cyclone-relative environmental helicity and the pathways to intensification in shear. *J. Atmos. Sci.*, **73**, 869-890.

Pendergrass, A.G., and H.E. Willoughby, 2009: Diabatically induced secondary flows in tropical cyclones. Part I: Quasi-steady forcing. *Mon. Wea. Rev.*, **137**, 805-821.

Peng, K., R. Rotunno, and G.H. Bryan, 2018. Evaluation of a time-dependent model for the intensification of tropical cyclones. *J. Atmos. Sci.*, **75**, 2125-2138.

Rappin, E.D., D.S. Nolan, and K.A. Emanuel, 2010: Thermodynamic control of tropical cyclogenesis in environments of radiative-convective equilibrium with shear. *Q. J. R. Meteorol. Soc.*, **136**, 1954-1971.

Rappin, E.D., and D.S. Nolan, 2012: The effect of vertical shear orientation on tropical cyclogenesis. *Q. J. R. Meteorol. Soc.*, **138**, 1035-1054.

Reasor, P.D., and M.T. Montgomery, 2001: Three-dimensional alignment and corotation of weak, TC-like vortices via linear vortex-Rossby-waves. *J. Atmos. Sci.*, **58**, 2306-2330.

Reasor, P.D., M.T. Montgomery, and L.D. Grasso, 2004: A new look at the problem of tropical cyclones in shear flow: vortex resiliency. *J. Atmos. Sci.*, **61**, 3-22.

Reasor, P.D., R. Rogers, and S. Lorsolo, 2013: Environmental flow impacts on tropical cyclone structure diagnosed from airborne Doppler radar composites. *Mon. Wea. Rev.*, **141**, 2949-2969.

Riemer, M., M.T. Montgomery, and M.E. Nicholls, 2010: A new paradigm for intensity modification of tropical cyclones: Thermodynamic impact of vertical wind shear on the inflow layer. *Atmos. Chem. Phys.*, **10**, 3163-3188.

Riemer, M., M.T. Montgomery, and M.E. Nicholls, 2013: Further examination of the thermodynamic modification of the inflow layer of tropical cyclones by vertical wind shear. *Atmos. Chem. Phys.*, **13**, 327-346.

Riemer, M., and F. Laliberté, 2015: Secondary circulation of tropical cyclones in vertical wind shear: Lagrangian diagnostic and pathways of environmental interaction. *J. Atmos. Sci.*, **72**, 3517-3536.

Rios-Berrios, R., C.A. Davis, and R.D. Torn and 2018: A hypothesis for the intensification of tropical cyclones under moderate vertical wind shear. *J. Atmos. Sci.*, **75**, 4149-4173.

Rios-Berrios, R., 2020: Impacts of radiation and cold pools on the intensity and vortex tilt of weak tropical cyclones interacting with vertical wind shear. *J. Atmos. Sci.*, **77**, 669-689.

Rogers, R.F., P.D. Reasor, J.A. Zawislak, and L.T. Nguyen, 2020: Precipitation processes and vortex alignment during the intensification of a weak tropical cyclone in moderate vertical shear. *Mon. Wea. Rev.*, **148**, 1899-1929.

Rotunno, R., and K.A. Emanuel, 1987: An airsea interaction theory for tropical cyclones. Part II: Evolutionary study using a nonhydrostatic axisymmetric numerical model. *J. Atmos. Sci.*, **44**, 542-561.

Ruppert, J.H., Jr., A.A. Wing, X. Tang, and E.L. Duran, 2020: The critical role of cloud-infrared radiation feedback in tropical cyclone development. *Proc. Natl. Acad. Sci.*, **117**, 27884-27892.

Schecter, D.A., and M. T. Montgomery, 2003: On the symmetrization rate of an intense geophysical vortex. *Dyn. Atmos. Oceans*, **37**, 55-88.

Schecter, D.A., and M.T. Montgomery, 2007: Waves in a cloudy vortex. *J. Atmos. Sci*, **64**, 314-337.

Schecter, D.A., 2011: Evaluation of a reduced model for investigating hurricane formation from turbulence. *Quart. J. Roy. Meteor. Soc.*, **137**, 155-178.

Schecter, D.A., 2016: Development and nondevelopment of binary mesoscale vortices into tropical cyclones in idealized numerical experiments. *J. Atmos. Sci.*, **73**, 1223-1254.

Schecter, D.A., 2020: Distinct intensification pathways for a shallow-water vortex subjected to asymmetric "diabatic" forcing. *Dyn. Atmos. Oceans*, **91**, 101156:1-25.

Schecter, D.A., and K. Menelaou, 2020: Development of a misaligned tropical cyclone. *J. Atmos. Sci.*, **77**, 79-111.

Stevenson, S.N., K.L. Corbosiero, and J. Molinari, 2014: The convective evolution and rapid intensification of Hurricane Earl (2010). *Mon. Wea. Rev.*, **142**, 4364-4380.

Tang, B., and K. Emanuel, 2012: A ventilation index for tropical cyclones. *Bull. Amer. Meteor. Soc.*, **93**, 1901-1912.

Tang, B.H., R. Rios-Berrios, J.J. Alland, J.D. Berman, and K.L. and Corbosiero, 2016: Sensitivity of axisymmetric tropical cyclone spinup time to dry air aloft. *J. Atmos. Sci.*, **73**, 4269-4287.

Tao, D., and F. Zhang, 2014: Effect of environmental shear, sea-surface temperature, and ambient moisture on the formation and predictability of tropical cyclones: An ensemble-mean perspective. *J. Adv. Model. Earth Syst.*, **6**, 384-404.

Vigh, J.L., and W.H. Schubert, 2009: Rapid development of the tropical cyclone warm core. *J. Atmos. Sci.*, **66**, 3335-3350.

Xu, J., and Y. Wang, 2015: A statistical analysis on the dependence of tropical cyclone intensification rate on the storm intensity and size in the North Atlantic. *Weather and Forecasting*, **30**, 692-701.

Xu, J., and Y. Wang, 2018: Dependence of tropical cyclone intensification rate on sea surface temperature, storm intensity, and size in the western North Pacific. *Weather and Forecasting*, **33**, 523-537.

Xu, J., Y. Wang, and C. Yang, 2019: Interbasin differences in the median and variability of tropical cyclone MPI in the northern hemisphere. *J. Geophys. Res. Atmos.*, **124**, 13714-13730.

Xu, J., Y. Wang, and Z.M. Tan, 2016: The relationship between sea surface temperature and maximum intensification rate of tropical cyclones in the North Atlantic. *J. Atmos. Sci.*, **73**, 4979-4988.

Zawislak, J., H. Jiang, G.R. Alvey, E.J. Zipser, R.F. Rogers, J.A. Zhang, and S.N. Stevenson, 2016: Observations of the structure and evolution of Hurricane Edouard (2014) during intensity change. Part I: Relationship between the thermodynamic structure and precipitation. *Mon. Wea. Rev.*, **144**, 3333-3354.

Zhang, J.A., P.G. Black, J.R. French, and W.M. Drennan, 2008: First direct measurements of enthalpy flux in the hurricane boundary layer: The CBLAST results. *Geophys. Res. Lett.*, **35**, L14813:1-4.

Group Name	SST (^{o}C)	Range of $tilt_0$ (km)	$N_{\rm LR}$, $N_{\rm HR}$	$N_{\rm IS}$, $N_{\rm ISPD}$, $N_{\rm DSPD}$	Featured Group Members	$tilt_0$, $\langle tilt \rangle$, $\langle r_m \rangle$ (km)
T26	26	0-367	9, 3	0, 4, 8	T26-LRA	365,98,66
					T26-HRA	367,—,—
					T26-HRB	182,48,54
T28	28	0-367	11, 23	3, 17, 14	T28-LRA	365,113,99
					T28-HRA	367,122,107
T30	30	0-367	9, 3	0, 4, 8	T30-LRA	365,80,68
					T30-HRA	367,95,69

TABLE 1. Summary of the numerical simulations. $N_{\rm LR/HR}$ denotes the number of low/high resolution simulations within a particular group. $N_{\rm IS/ISPD/DSPD}$ denotes the number of simulations initialized with the IS/ISPD/DSPD tilting procedure. All other variables appearing in the table header are defined in the main text.

1239

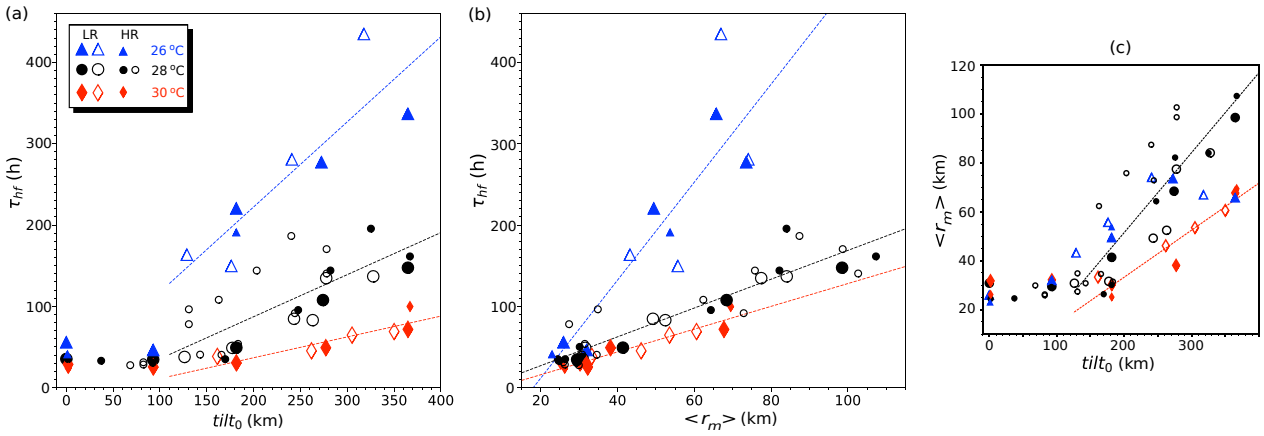

Figure 1: (a) Length of the HFP ($\tau_{\rm hf}$) versus the initial tilt magnitude ($tilt_0$). Filled (empty) symbols correspond to simulations having tilts initially generated by the DSPD (IS or ISPD) method. The color and shape of each symbol corresponds to the SST, and the relative size corresponds to model-resolution as shown in the legend, which applies to all subfigures. The dashed lines are linear regressions for the color-matched data points (belonging to distinct SST groups) with $tilt_0 > 100$ km. (b) Relationship between $\tau_{\rm hf}$ and the HFP time-averaged radius of maximum surface wind speed $\langle r_m \rangle$. Each dashed line is a linear regression as in (a), but covers all data points within the pertinent SST group. (c) Relationship between $\langle r_m \rangle$ and $tilt_0$ [the abscissas in (b) and (a)]. The linear regressions are as in (a), but are drawn only for groups T28 and T30.

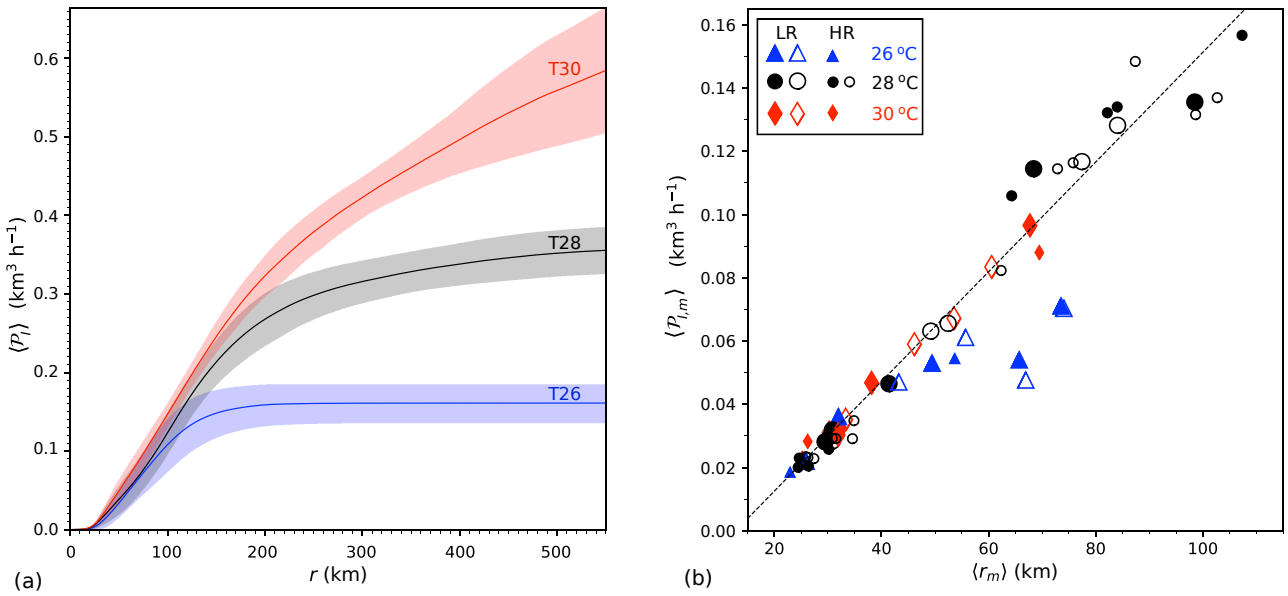

Figure 2: (a) HFP time average of the precipitation rate integrated over a surface vortex centered disc of radius r for simulation groups T26 (blue), T28 (black) and T30 (red). Each thin dark line represents a group mean, and the thick light background curve extends vertically from one local standard deviation below the mean, to one above. (b) HFP time average of the precipitation rate integrated over a surface vortex centered disc of radius $1.2r_m(t)$ versus the HFP time average of r_m. The symbols are as in Fig. 1, and the dashed line is the linear regression for groups T28 and T30 combined.

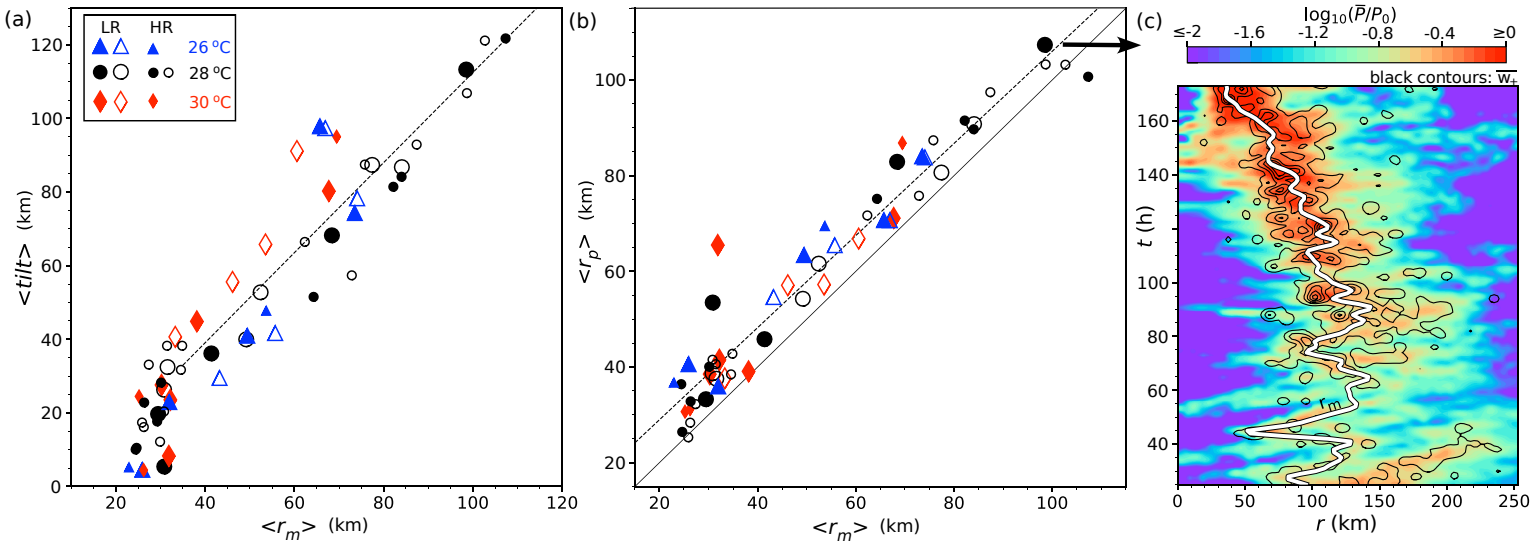

Figure 3: (a) Relationship between the HFP time-averaged tilt magnitude $\langle tilt \rangle$ and $\langle r_m \rangle$. The symbols are as in Fig. 1; the dashed line is a linear regression with a correlation coefficient of 0.87 for data with $\langle r_m \rangle \geq 35$ km from all SST-groups. (b) Relationship between the HFP time-averaged precipitation radius $\langle r_p \rangle$ and $\langle r_m \rangle$. The symbols are as in (a), but the dashed linear regression (with a correlation coefficient of 0.97) covers all values of $\langle r_m \rangle$. The solid line corresponds to $\langle r_p \rangle = \langle r_m \rangle$. (c) Radius-time Hovmöller plots of the logarithm of $\bar{P}$ normalized to $P_0 = 1.25$ cm h^{-1} (color), and $\overline{w_+}$ (contours) during the HFP of simulation T28-LRA, which corresponds to the data point at the tail of the black arrow in (b). The $\overline{w_+}$-contours are spaced 0.15 m s^{-1} apart, starting at 0.05 m s^{-1} on the periphery of a nested set. The white curve with black trim shows $r_m(t)$.

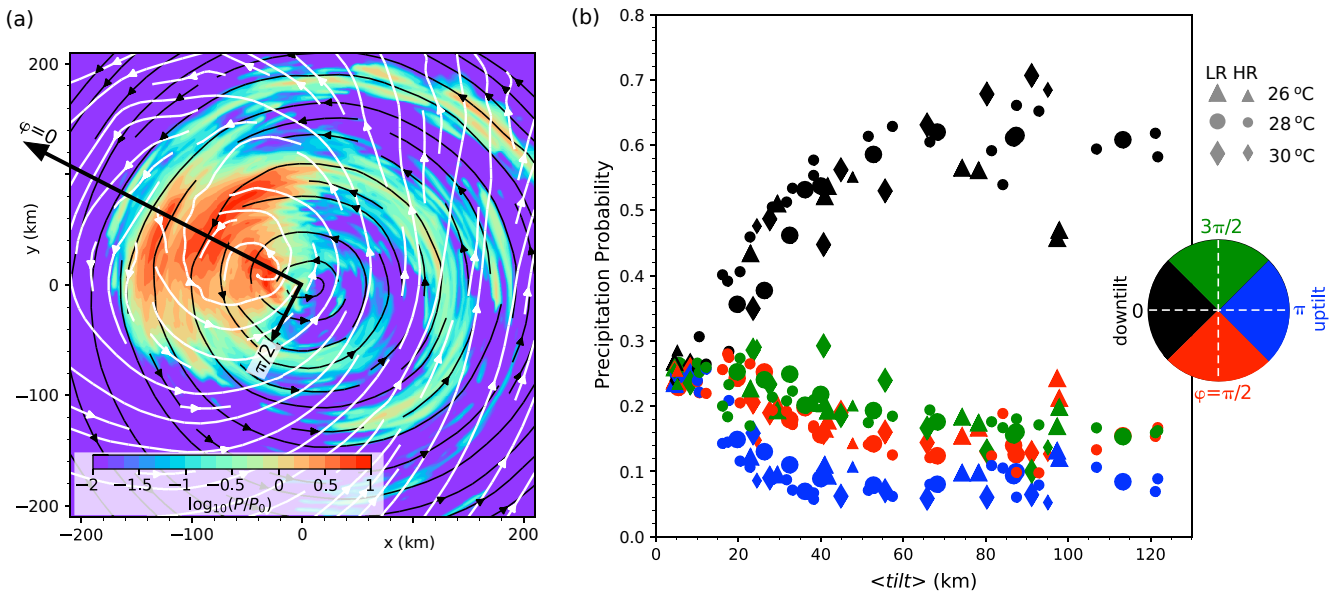

Figure 4: (a) Snapshot of the logarithm of the precipitation rate P normalized to $P_0 = 0.5$ cm h^{-1} within a typical tropical cyclone (from T28-HRA) during its HFP. Middle tropospheric ($z \approx 7.7$ km, white) and lower tropospheric ($z \approx 1.2$ km, black) streamlines are superimposed over the distribution. The long thick black arrow points in the direction of the tilt vector, which is parallel to the $\varphi = 0$ axis in the polar coordinate system used to construct the PPD. (b) The precipitation probability $\langle \hat{\mathcal{P}}_\varphi \rangle$ in each quadrant of the surface vortex, plotted against the time averaged tilt magnitude. As indicated by the inset, black/blue data correspond to the downtilt/uptilt quadrant, whereas red/green data correspond to the quadrant on the left/right side of the tilt vector. The symbol shapes and sizes respectively correspond to the SST and model resolution as in Fig. 1, but no distinction is made between symbols representing simulations with different initialization procedures.

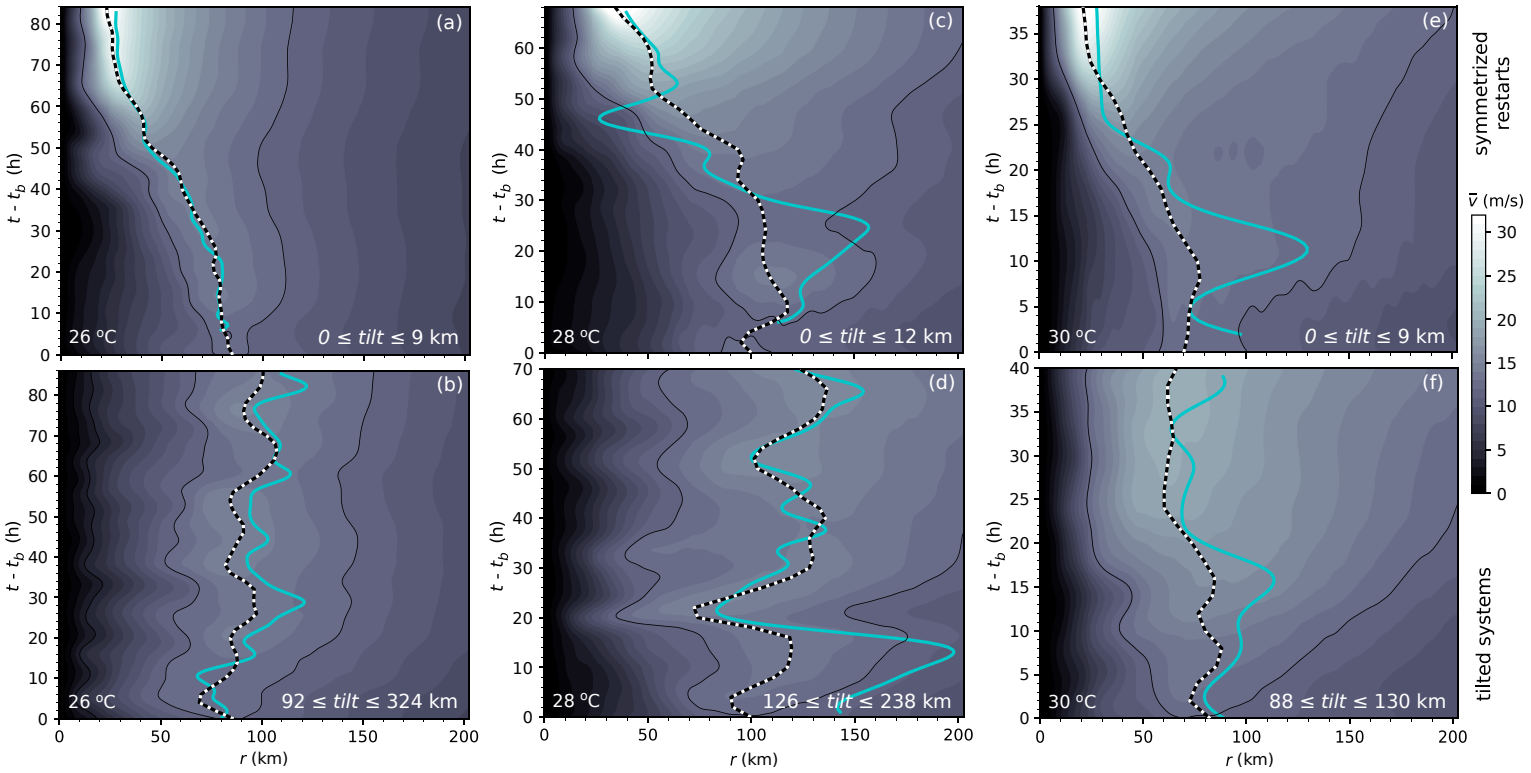

Figure 5: (a) Evolution of $\bar{v}$ at $z = 50$ m (shaded contour plot) in a symmetrized restart of T26-LRA at the beginning of the HFP. The black reference contours correspond to 12 m s^{-1}, which is just under the maximum of $\bar{v}$ at the start of the HFP. The black-and-white dashed (solid cyan) curve traces r_m (r_p). The bottom-right corner of the graph shows the range of the tilt magnitude during the depicted time frame. (b) As in (a), but for T26-LRA without modification. (c,d) As in (a,b) but for T28-LRA. (e,f) As in (a,b) but for T30-LRA. The greyscale to the right is for all contour plots. All plotted variables are Gaussian smoothed in t with a standard deviation parameter of 2 h.

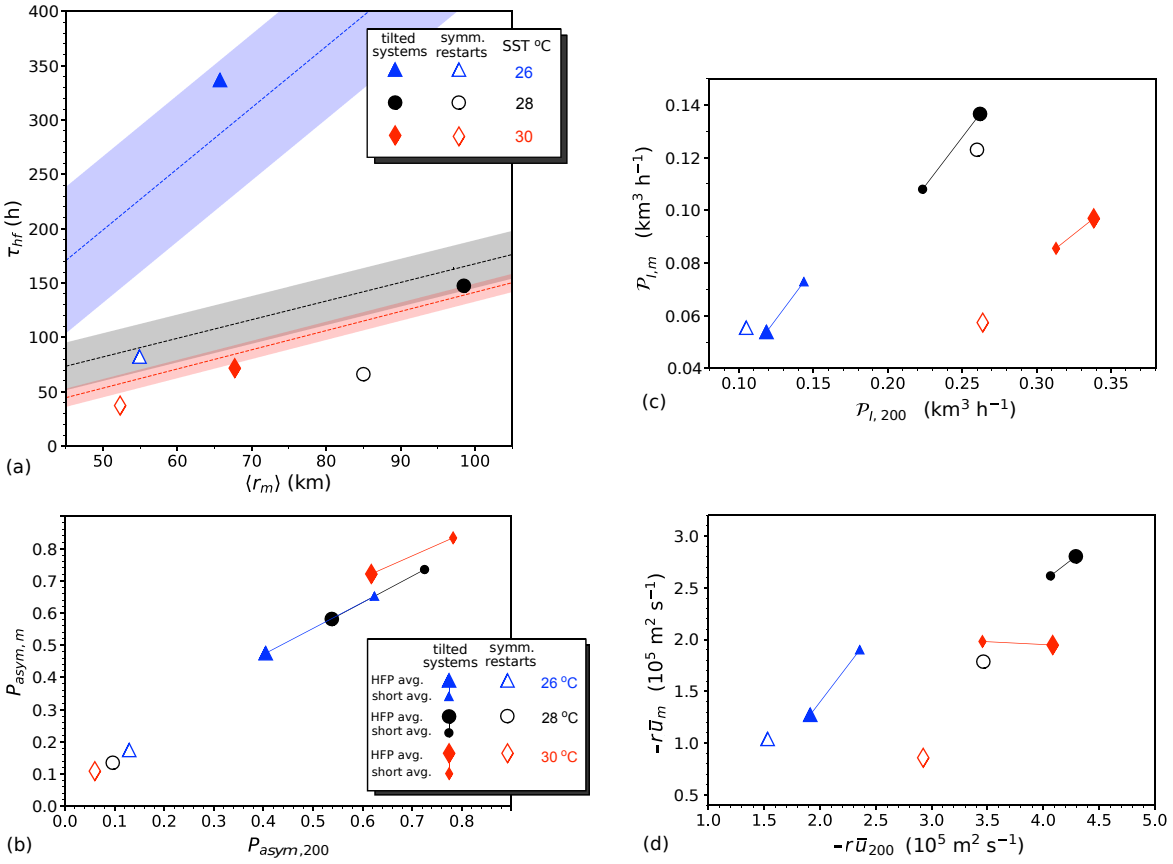

Figure 6: (a) Length of the HFP versus $\langle r_m \rangle$ for the tilted tropical cyclones in simulations T26-LRA, T28-LRA and T30-LRA (filled symbols), and for their counterparts in the initially symmetrized restarts (empty symbols). Each slanted dashed line is a linear regression obtained using data from all of the tilted tropical cyclone simulations in a particular SST-group with $\langle r_m \rangle \geq 40$ km; the thick color-matched background line extends vertically between plus and minus one root-mean-square deviation of this data from the regression line. The colors of all symbols and lines indicate the SST as shown in the legend. (b) Time averages of P_{asym} evaluated with a disc radius a equal to (vertical axis) $1.2r_m(t)$ and (horizontal axis) 200 km for the tilted tropical cyclones and their initially symmetrized counterparts. Large (small) symbols correspond to HFP (shorter) time averages, as explained in the main text. The color scheme follows that in (a). The legend applies to (b)-(d). (c) As in (b) but for time averages of $\mathcal{P}_I(a,t)$. (d) As in (b) but for the inward mass-flux in the nominal boundary layer, measured by the vertical average of $-r\bar{u}$ from the surface to $z \approx 1$ km, evaluated at (vertical axis) $r = 1.2r_m(t)$ and (horizontal axis) 200 km.

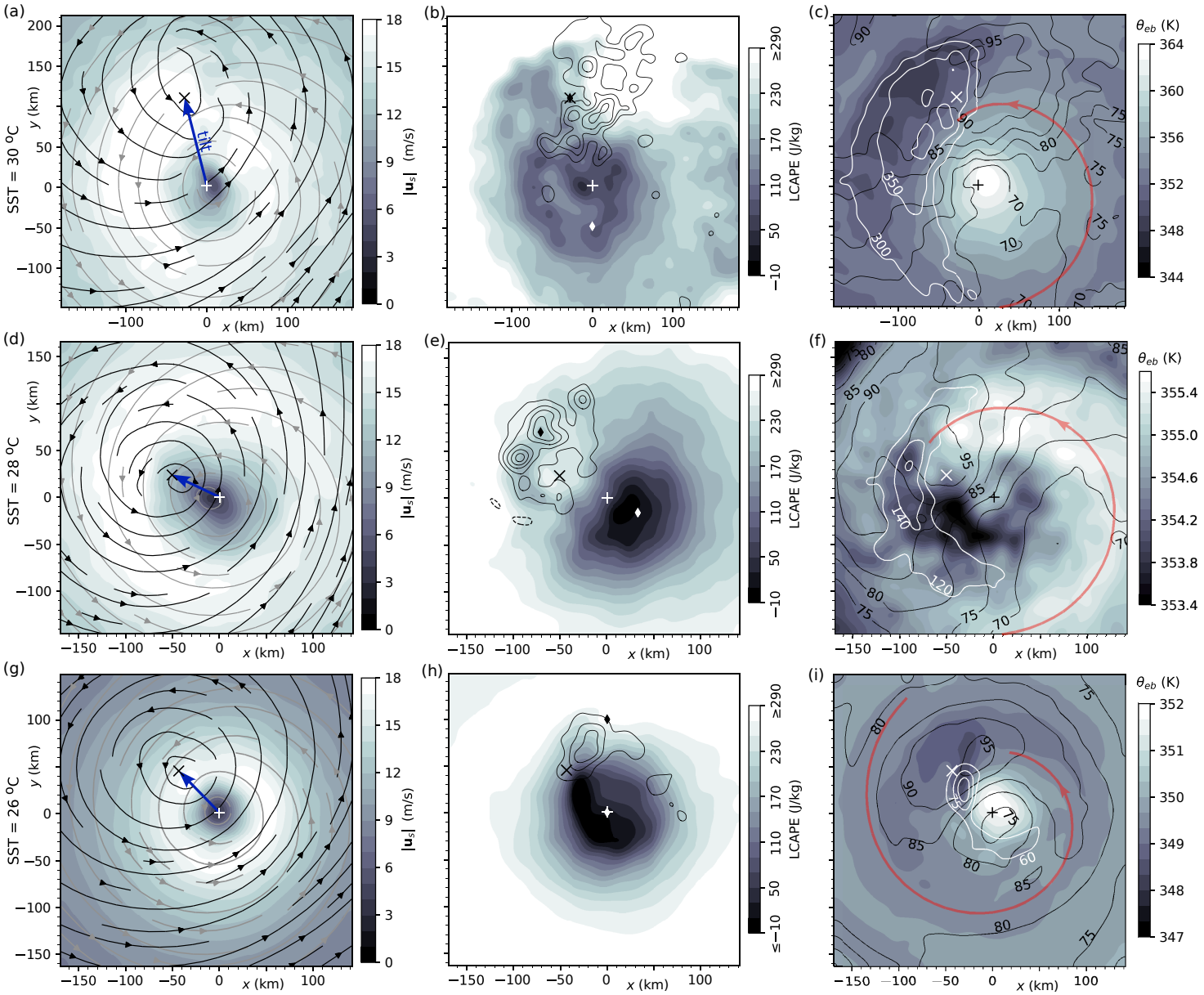

Figure 7: **(a-c)** Depiction of the tilted tropical cyclone in T30-HRA, averaged over a 6-h interval starting in the midst of the HFP, well before fast spinup. (a) Horizontal streamlines in the middle troposphere (black lines) and boundary layer (grey lines), superimposed over the near-surface ($z = 25$ m) horizontal wind speed $|\mathbf{u}_s|$ in an earth-stationary reference frame. (b) Vertical velocity (w) contours in the upper troposphere ($z = 8.9$ km) superimposed over the distribution of LCAPE [Eq. (5)]. (c) Lower–middle tropospheric relative humidity $\mathcal{H}$ (black contours, %), the surface enthalpy flux F_k where peaked (white contours, W m^{-2}), and the boundary layer equivalent potential temperature θ_{eb} (greyscale). A faint red boundary layer streamline connected to the convection zone is shown for reference. **(d-f)** As in (a-c), but for T28-HRA. **(g-i)** As in (a-c) but for T26-HRA. In each panel, the + marks the 6-h time-averaged surface vortex center ($\mathbf{x}_{cs}$), where the origin of the x-y Cartesian coordinate system is placed. The × marks the 6-h time average of the middle tropospheric vortex center ($\mathbf{x}_{cm}$). The tilt vector points from + to ×, as illustrated by the blue arrows in the left column. Positive (solid) and negative (dashed) w-contours are spaced 0.5 m s^{-1} apart starting from ±0.5 m s^{-1} in (b,e) on the outer rim of a nested set, and from ±0.25 m s^{-1} in (h); downdrafts are strong enough to be contoured only in (e). The boundary layer streamlines and θ_{eb} are obtained from fields averaged over $z \leq 1$ km. The middle tropospheric streamlines are obtained from the average of the horizontal velocity field over $7.3 \leq z \leq 8.1$ km. $\mathcal{H}$ is averaged over $2.3 \leq z \leq 7.7$ km. All contoured fields (filled or unfilled) are Gaussian smoothed with a standard deviation parameter of 6.25 km in both x and y. The black/white diamonds in (b,e,h) mark the sounding locations for the top/bottom row of Fig. 10.

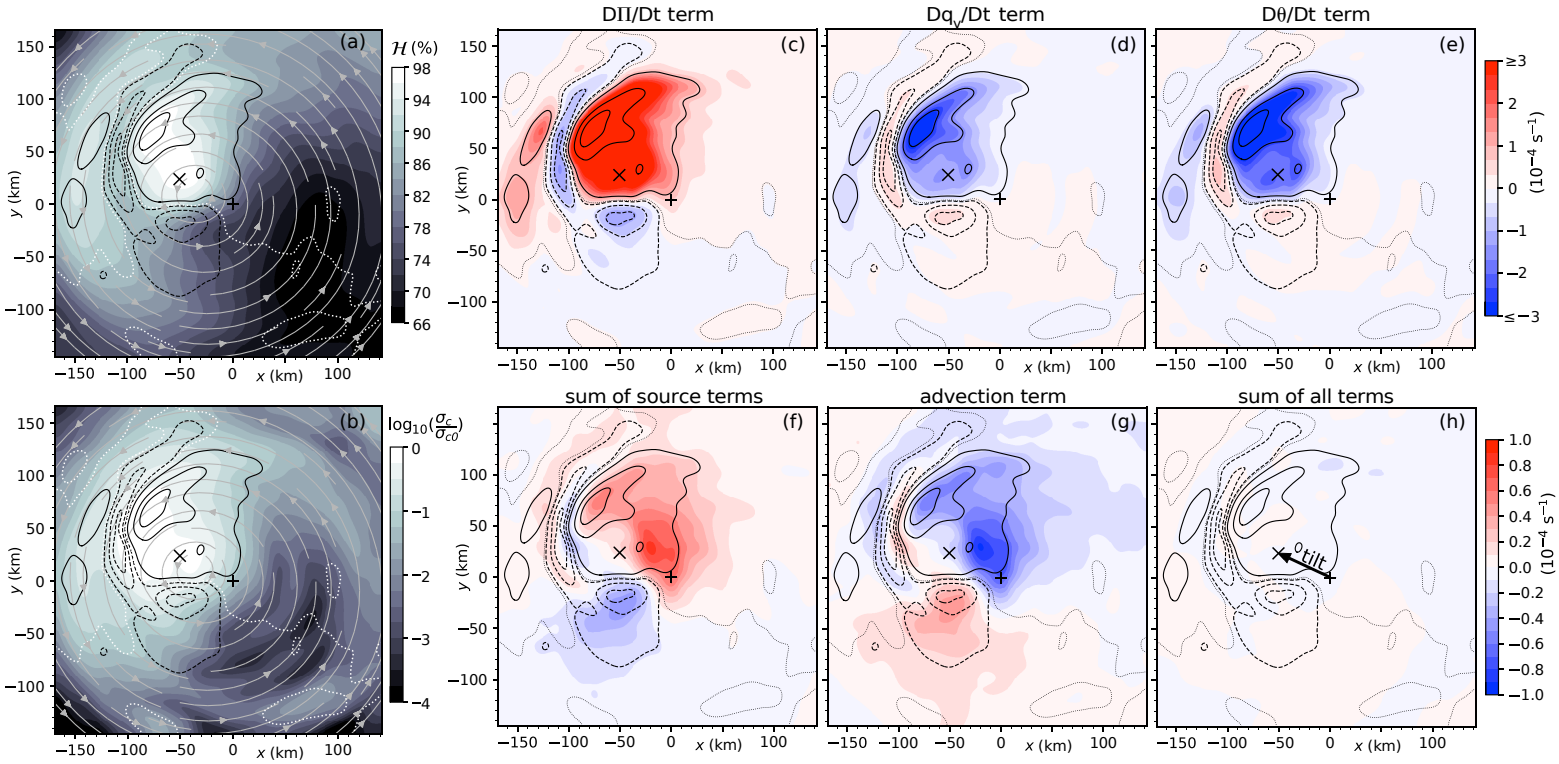

Figure 8: Illustration of the lower–middle tropospheric moisture dynamics occurring in the tropical cyclone of simulation T28-HRA while moderately tilted during a selected 6-h segment of the HFP (corresponding to that in Figs. 7d-f). All fields are time-averaged over this segment and vertically averaged (except for σ_c, which is a vertical integral) as explained in the main text. The surface and middle tropospheric vortex centers are respectively marked by + and × as in Fig. 7. (a) Reference plot of relative humidity $\mathcal{H}$ (greyscale), w-contours (black and white), and streamlines of horizontal velocity $\mathbf{u}$ (grey with arrows). Positive (solid black) w-contours are from the set $\{0.15, 0.68, 1.13\}$ m s^{-1}, negative (dashed black) w-contours are from the set $-\{0.03, 0.15, 0.25\}$ m s^{-1}, and the zero w-contours are represented by the dotted white lines. (b) Reference plot of the logarithm of the z-integrated hydrometeor mass density σ_c normalized to $\sigma_{c0} = 10$ kg m^{-2}. Contours and streamlines are as in (a). (c-e) Formal positive and negative source terms contributing to $\partial\mathcal{H}/\partial t$ on the right-hand side of Eq. (4) attributable to changes of (c) pressure, (d) water vapor, and (e) potential temperature in air parcels. (f) The sum of all positive and negative source terms in (c-e). (g) The advection term on the right-hand side of Eq. (4). (h) The sum of the advection and source terms. Contours in (c-h) are as in (a), except for the $w = 0$ contour being black instead of white. The colorbar to the right of (e) applies to (c-e), whereas the colorbar to the right of (h) applies to (f-h). All plotted fields (excluding $\mathbf{u}$) are Gaussian smoothed in x and y with a 6.25-km standard deviation parameter.

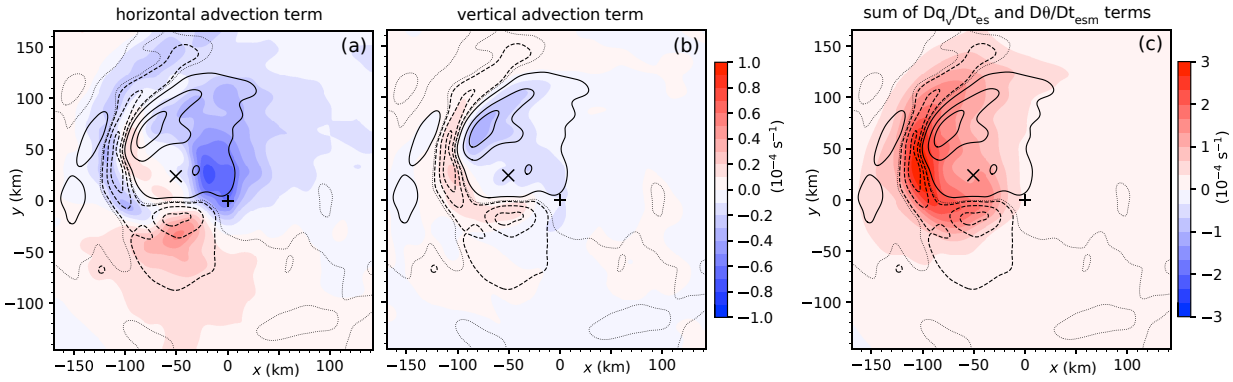

Figure 9: (a,b) Contributions to the 3D advection term in Fig. 8g from (a) horizontal and (b) vertical advection. (c) Sum of contributions to the Dq_v/Dt and $D\theta/Dt$ terms in Figs. 8d and 8e from evaporation (subscript-e), sublimation (subscript-s) and melting (subscript-m).

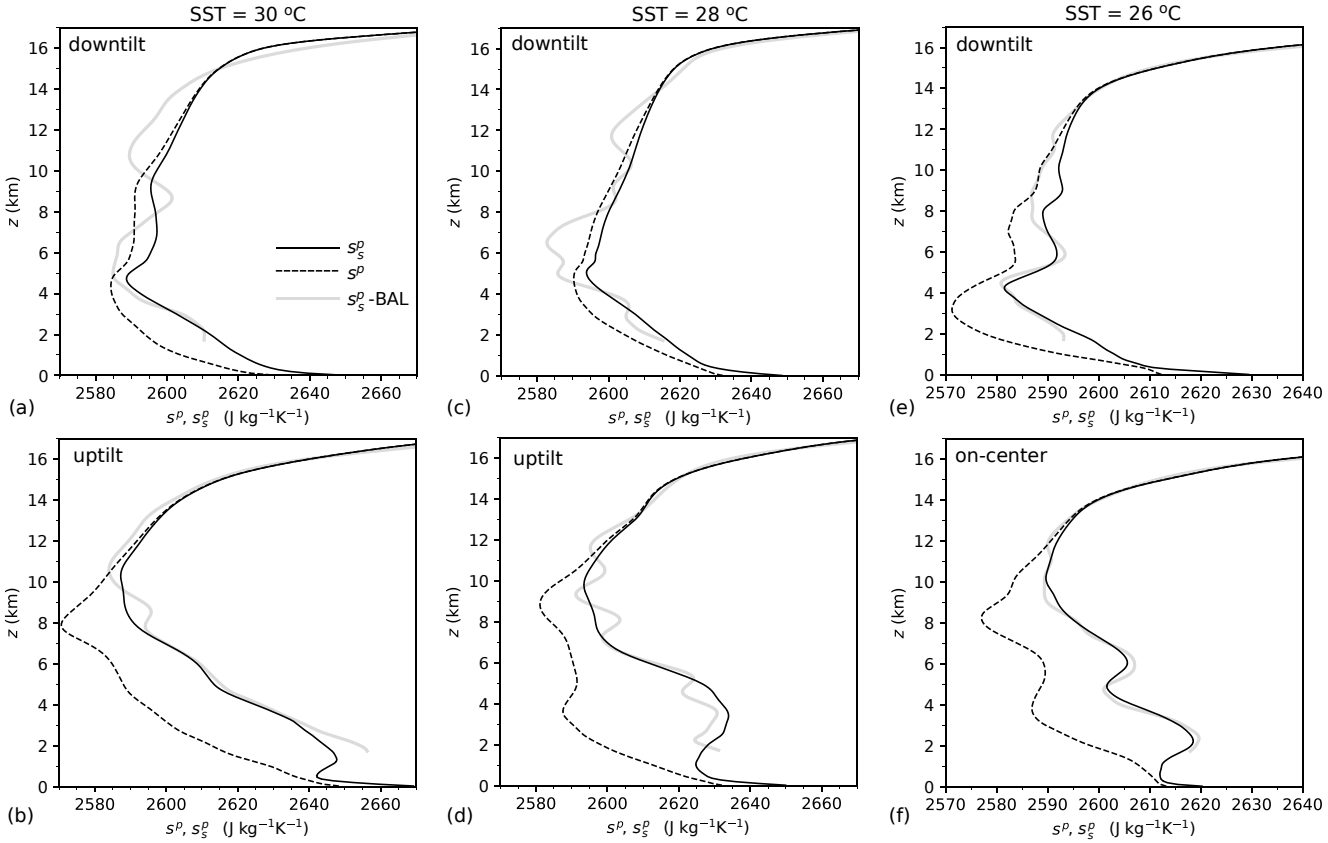

Figure 10: (a,b) Vertical profiles of the entropy s^p (dashed black) and saturation entropy s_s^p (solid black) found in (a) downtilt and (b) uptilt regions of the inner core of the tropical cyclone in simulation T30-HRA, averaged over the 6-h time period in Fig. 7b. Specifically, the two profiles are taken in the vicinities of (a) the black diamond and (b) the white diamond in the aforementioned figure. The solid grey curves starting above the boundary layer show s_s^p when the pressure and potential temperature fields are adjusted to precisely satisfy the equations of nonlinear balance (BAL) for the particular ζ-distribution of the misaligned vortex. (c,d) As in (a,b) but for entropy profiles taken from the 6-h time period of simulation T28-HRA in Fig. 7e, and at the diamonds (black/white for c/d) in the same figure. (e,f) As in (a,b) but for entropy profiles taken from the 6-h time period of simulation T26-HRA in Fig. 7h, and at the diamonds (black/white for e/f) in the same figure. Note that central profiles are shown instead of uptilt profiles in (f).

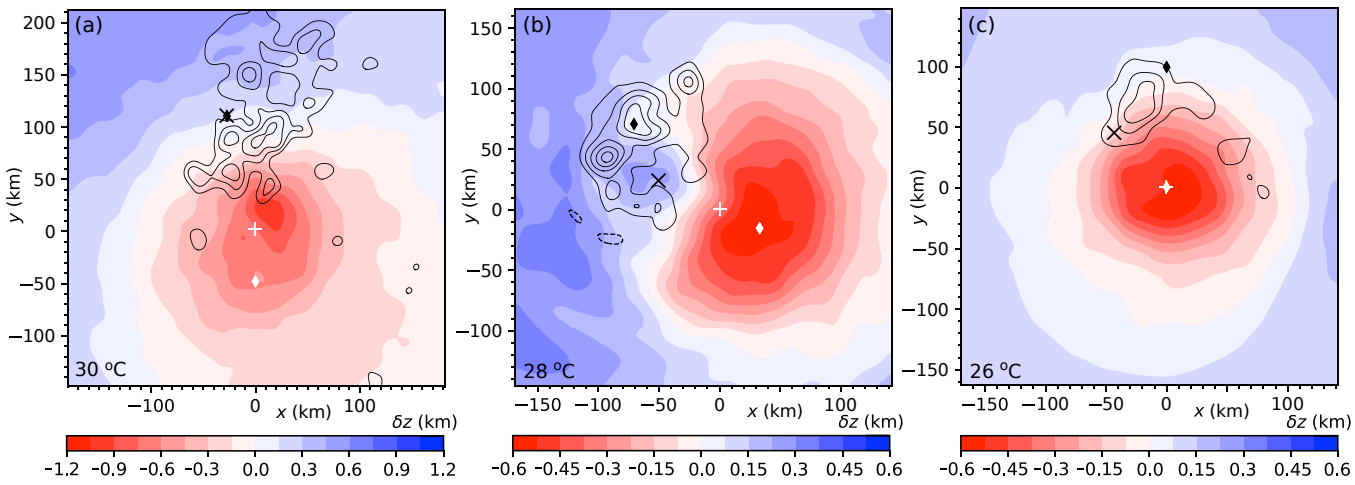

Figure 11: (a) Height minus $z_m = 4.1$ km (denoted δz) of the $\theta = 320.8$-K isosurface of the tilted tropical cyclone in simulation T30-HRA, averaged over the 6-h time interval represented by Figs. 7a-c. (b) As in (a) but for the $\theta = 321.6$-K isosurface of the tilted tropical cyclone in simulation T28-HRA over the 6-h interval in Figs. 7d-f. (c) As in (a) but for the $\theta = 321.6$-K isosurface of the tilted tropical cyclone in simulation T26-HRA over the 6-h interval in Figs. 7g-i, and with $z_m = 4.4$ km. The black w-contours, diamonds, + and $\times$ are as in Figs. 7b, 7e and 7h for (a), (b) and (c) respectively. Note the inversion of the usual blue-to-red colormap.

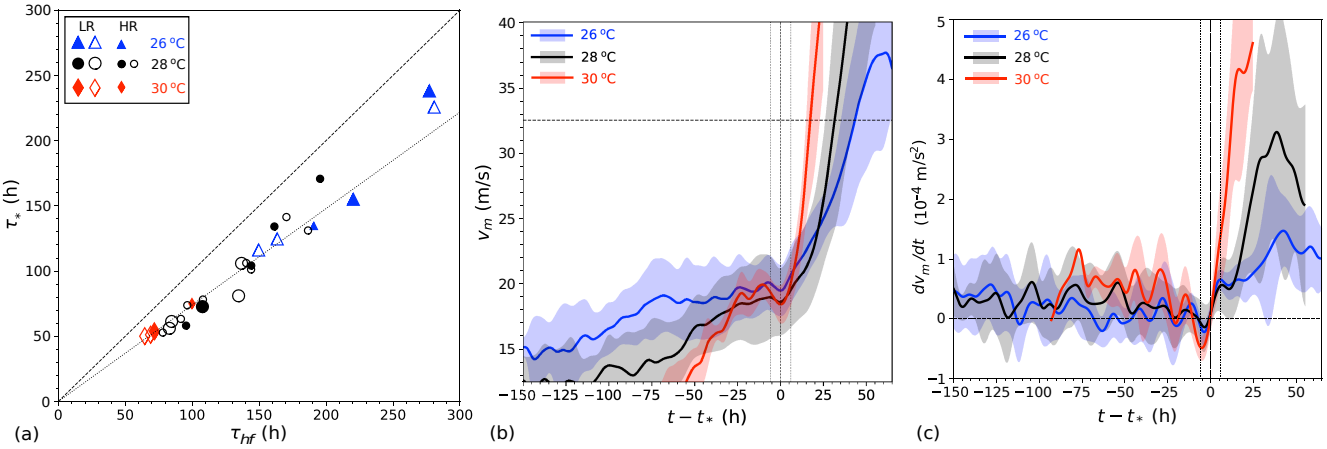

Figure 12: (a) Time interval between the beginning of the HFP and the transition to fast spinup (τ_*) versus the length of the HFP ($\tau_{\rm hf}$) for simulations that meet the rigid criteria for exhibiting a transition. Symbols are as in Fig. 1. The dashed (dotted) line corresponds to $\tau_* = \kappa\tau_{\rm hf}$, in which $\kappa = 1$ (0.74). (b) Time series of v_m for the simulations in (a). Each thin curve represents the mean for a particular SST-group (see legend), whereas the thick semitransparent curves extend vertically from minus-one to plus-one standard deviation from the mean. The dashed horizontal line corresponds to v_m at the end of the HFP, the dashed vertical line corresponds to the transition time $t = t_*$, and the dotted vertical lines correspond to $t = t_* \pm 6$ h. (c) As in (b) but for the time series of dv_m/dt, and with the dashed horizontal line corresponding to an intensification rate of zero. The curves representing SSTs of 28 and 30 ^{o}C are truncated on the right approximately when the last group member completes its HFP.

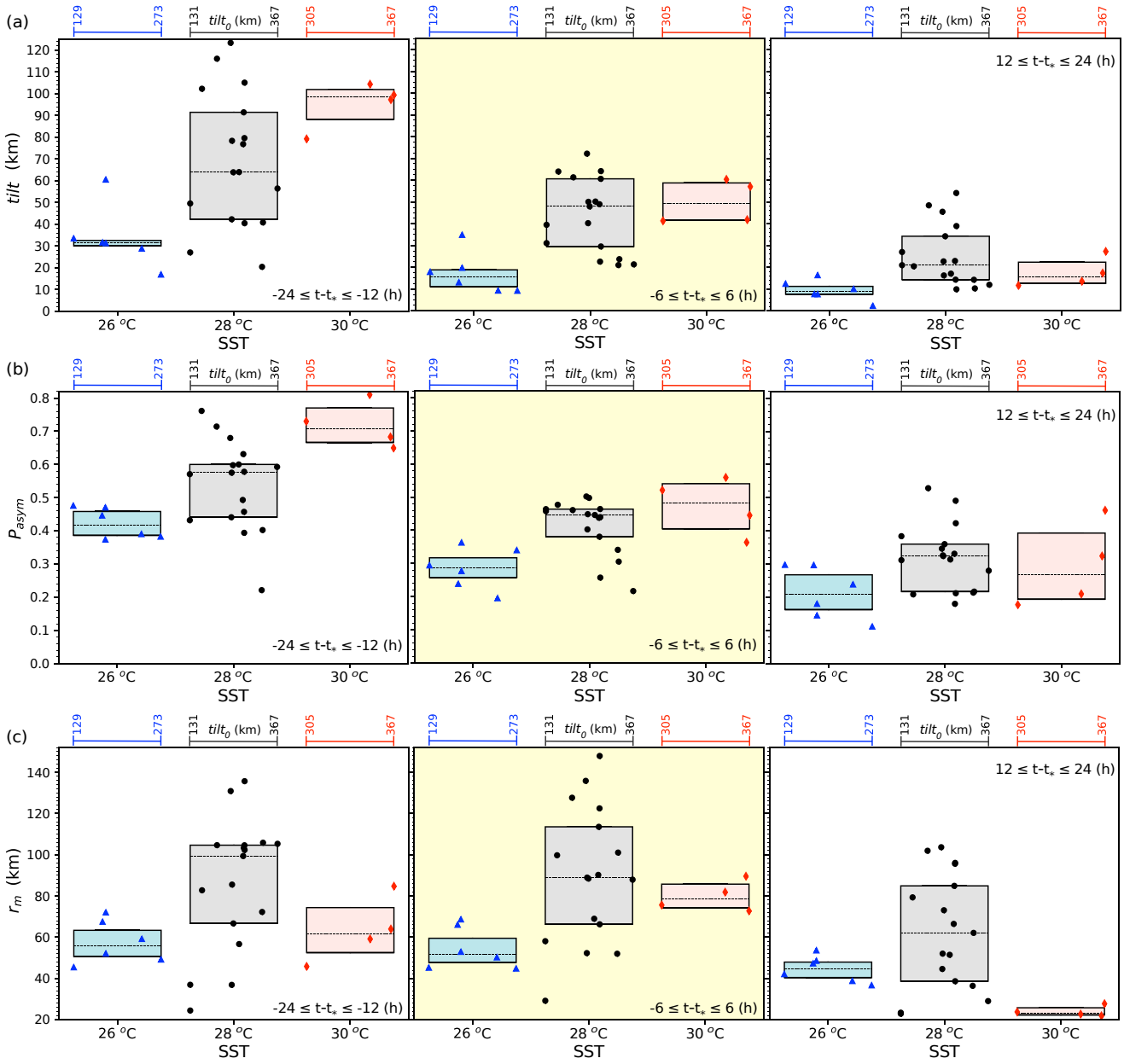

Figure 13: Evolution of (a) the tilt magnitude, (b) the precipitation asymmetry and (c) r_m for systems undergoing transitions to fast spinup. Plots highlighted with yellow backgrounds correspond to the 12-h interval centered at the transition time t_*. All other facets of this figure are explained in the main text.

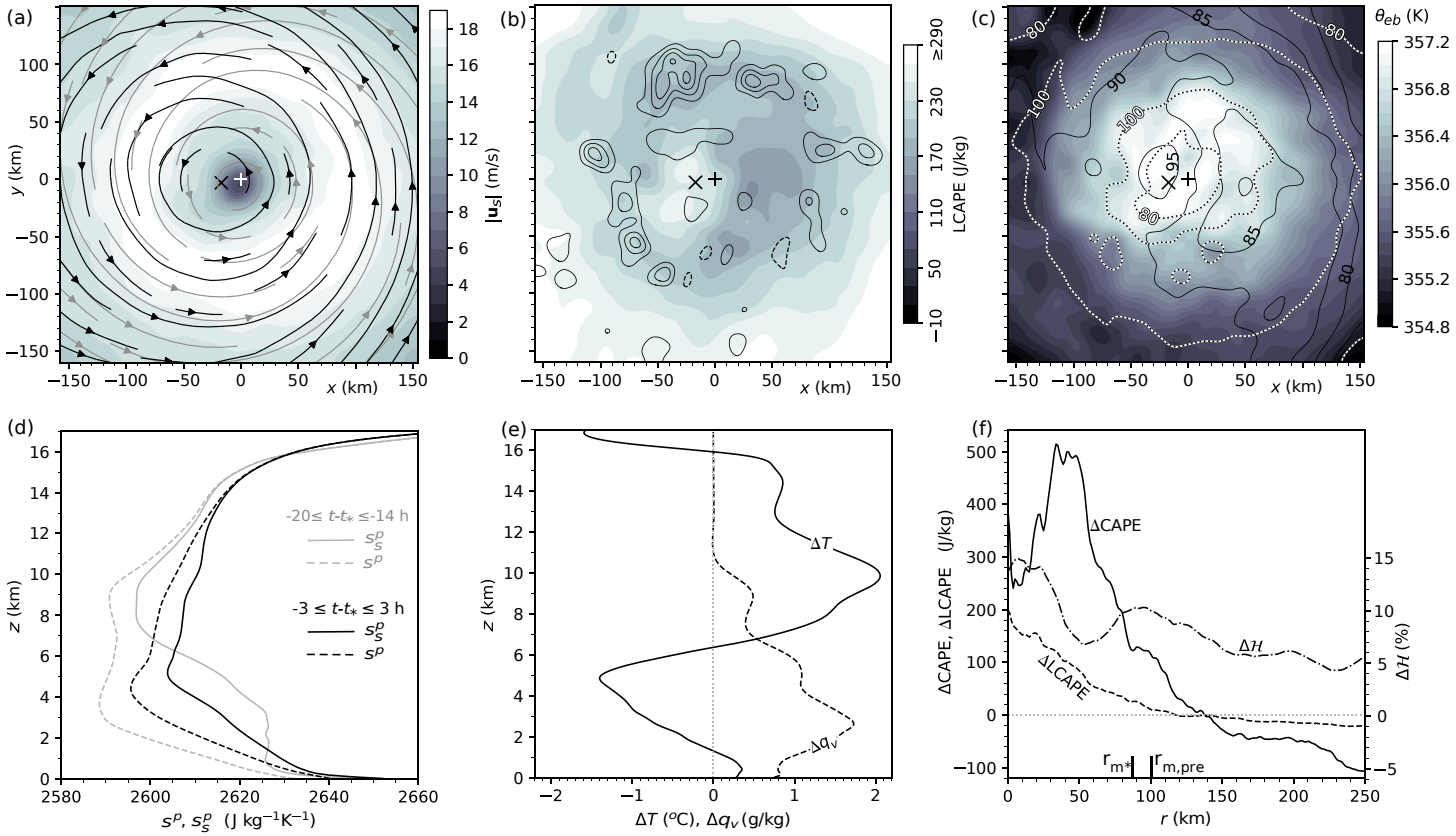

Figure 14: **(a-c)** Depiction of simulation T28-HRA during a 6-h period centered at the transition time t_*, similar to that shown for the pre-transitional time period starting 20 hours earlier in Figs. 7d-f. Plotting conventions slightly differ in that the top of the greyscale for $|\mathbf{u}_s|$ in (a) is extended to 19 m s^{-1}, w-contours in (b) are spaced 0.25 m s^{-1} apart, the greyscale for θ_{eb} in (c) is shifted upward and stretched, and the F_k-contours in (c) have alternating segments of black and white. **(d)** Inner core vertical profiles of the entropy s^p and saturation entropy s_s^p in the pre-transitional (grey) and transitional (black) states of simulation T28-HRA. **(e)** Changes (denoted by Δ) in the temperature T and water vapor mixing ratio q_v corresponding to the entropy changes from the pre-transitional to transitional states shown in (d). **(f)** Changes in the azimuthally averaged radial profiles of deep-layer CAPE, LCAPE and lower–middle tropospheric relative humidity ($\mathcal{H}$ averaged between $z = 2.3$ and 7.7 km) from the pre-transitional to transitional states of the simulation. Extended ticks on the bottom of the graph show r_m during these two states; i.e., before (pre) and at ($*$) the transition.

(a)

	26 ºC	28 ºC	30 ºC
$\mathcal{H}^c_-$ (%)	83.8 ± 4.5	78.4 ± 5.2	72.5 ± 3.0
$\mathcal{H}^c_*$	91.3 ± 3.3	83.7 ± 2.6	80.5 ± 2.9
LCAPE$^c_-$ (J/kg)	108 ± 42	92 ± 52	58 ± 28
LCAPE$^c_*$	155 ± 22	163 ± 44	184 ± 34
CAPE$^c_-$ (J/kg)	1031 ± 93	1826 ± 200	2553 ± 345
CAPE$^c_*$	1022 ± 132	1951 ± 130	2603 ± 210
F^c_{k-} (W/m^2)	75 ± 26	176 ± 55	348 ± 49
F^c_{k*}	68 ± 20	148 ± 44	283 ± 18
P^c_- (mm/h)	4.3 ± 0.9	4.2 ± 1.7	4.5 ± 0.2
P^c_*	4.7 ± 0.8	4.1 ± 1.4	4.1 ± 0.3
$tilt_-$ (km)	34 ± 13	69 ± 30	95 ± 10
$tilt_*$	17 ± 9	44 ± 16	50 ± 9

(b)

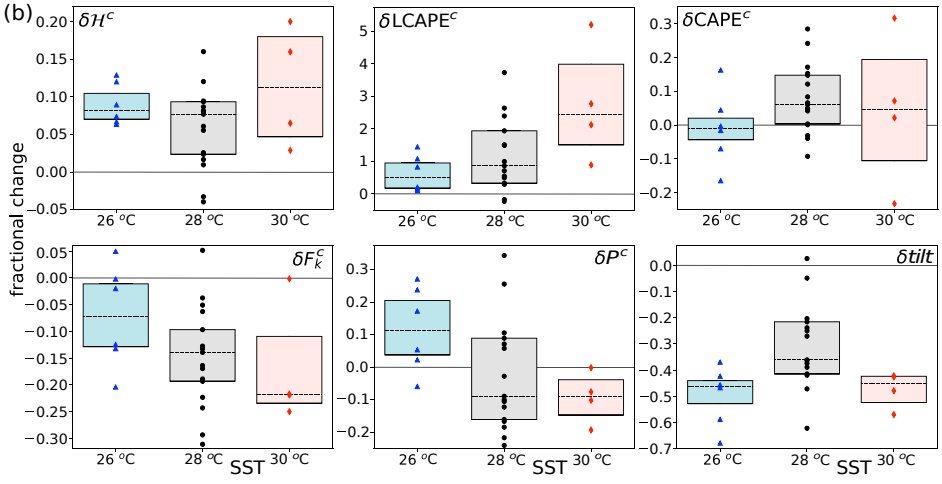

Figure 15: (a) Table showing the pre-transitional ($-$) and transitional ($*$) values of various core moist-thermodynamic parameters and the tilt magnitude. Mean values plus-or-minus the standard deviations are shown in separate columns for each SST-segregated simulation group. (b) The fractional change of each parameter (specified near the top of each panel) in going from the pre-transitional to transitional state. Each color-filled box in a given panel extends vertically from the first to third quartile of the data set for the SST printed underneath. The median is represented by the dashed horizontal line. Small symbols (triangles, circles and diamonds) show individual data points, excluding no more than a few outliers from group T28.

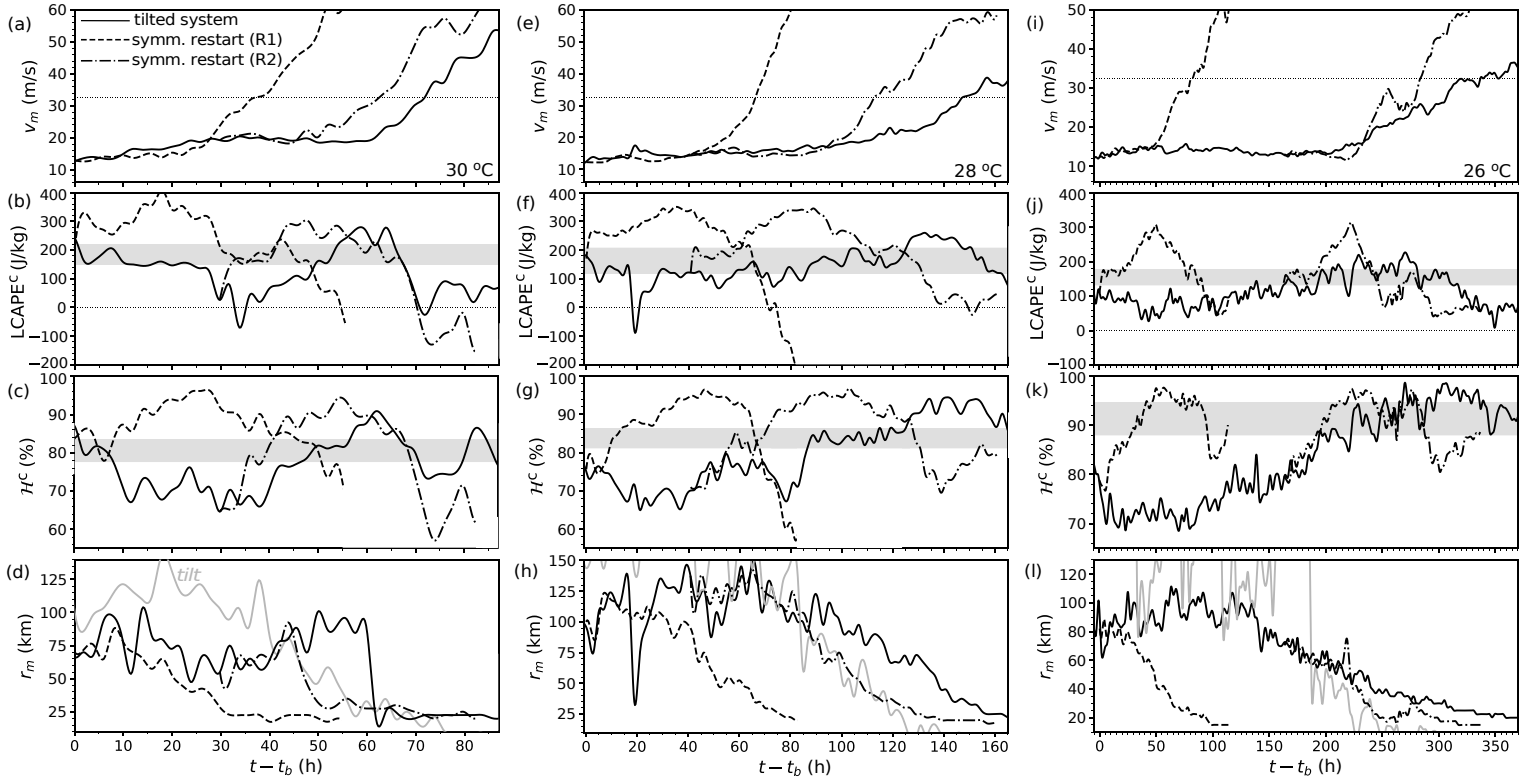

Figure 16: (a-d) Time series of (a) v_m, (b) LCAPE^c, (c) $\mathcal{H}^c$ and (d) r_m for simulation T30-LRA (solid black) and symmetrized restarts at the beginning (dashed) and at a later stage (dash-dotted) of the HFP. The dotted horizontal line in (a) corresponds to v_m at the end of the HFP. The dotted line in (b) corresponds to zero LCAPE^c. The grey horizontal bars in (b) and (c) are centered at the group-mean transitional values of the plotted moist-thermodynamic variables (see Fig. 15a), and are two standard deviations wide in the vertical dimension. The solid grey curve in (d) shows the tilt magnitude in T30-LRA. (e-h) As in (a-d) but for simulation T28-LRA. (i-l) As in (a-d) but for simulation T26-LRA.

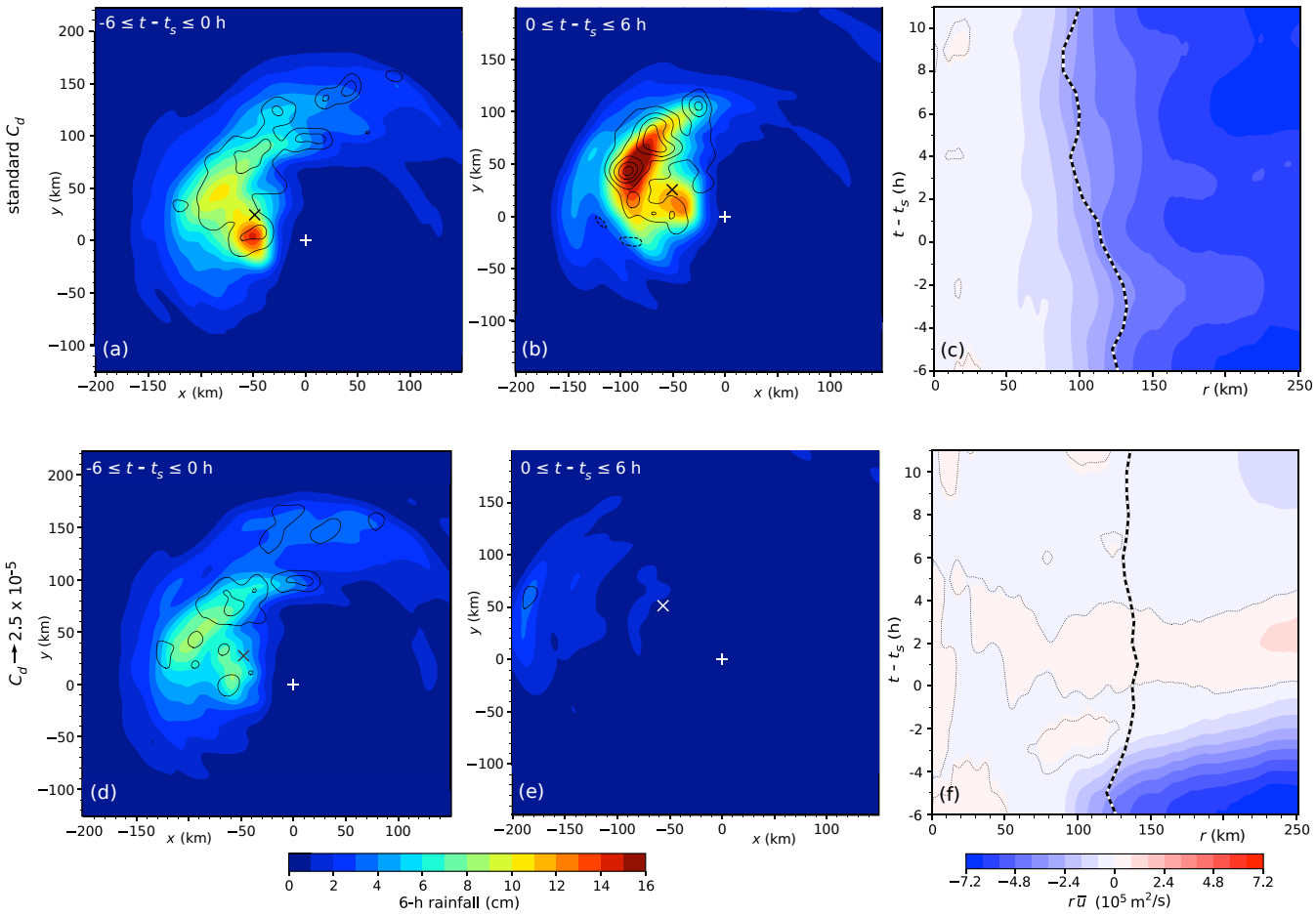

Figure A1: (a) The accumulated rainfall (color) and time-averaged w-contours over the interval $-6 \leq t - t_s \leq 0$ h in simulation T28-HRA. The w-contour levels are as in Fig. 7e. Both the rainfall and w fields are horizontally smoothed over an approximate 6.25 km radius. As usual, the + and × respectively mark the time-averaged rotational centers of the surface and middle tropospheric circulations. (b) As in (a) but for the interval $0 \leq t - t_s \leq 6$ h. (c) Evolution of the radial distribution of the effective radial mass flux ($r\bar{u}$) averaged over height in a 1-km deep boundary layer. The black-and-white dashed line is the radius of maximum height-averaged $\bar{v}$ in the boundary layer. (d-f) As in (a-c) but for a restart with $C_d \rightarrow 2.5 \times 10^{-5}$.

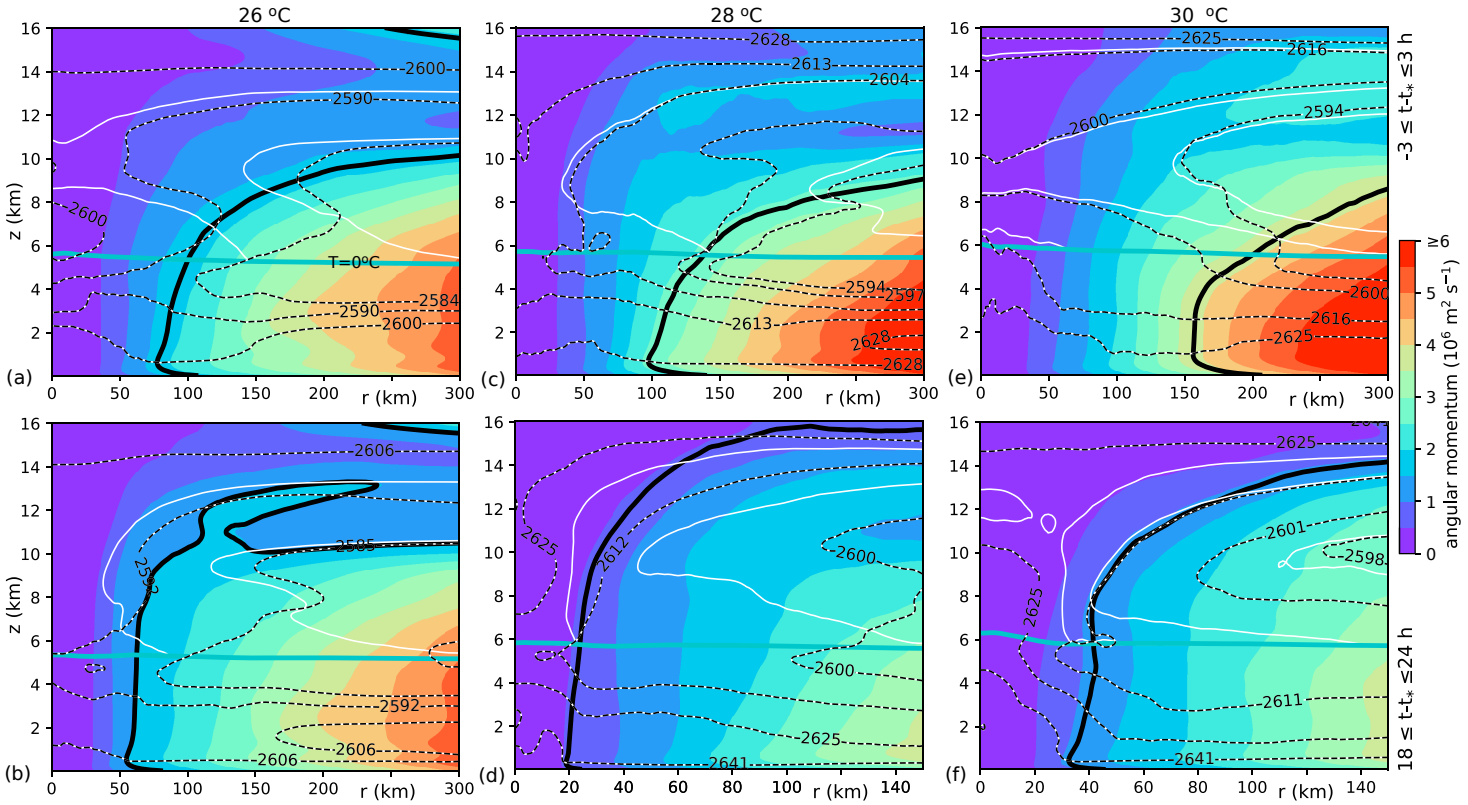

Figure B1: (a) Saturation entropy that assumes liquid-only condensate (dashed black-and-white contours; J kg^{-1} K^{-1}) and absolute angular momentum ($r\bar{v} + fr^2/2$, color) in simulation T26-HRB, averaged in azimuth and over a 6-h interval centered at the time t_* of the transition to fast spinup. The solid white lines above the freezing level (thick cyan line) are saturation entropy contours assuming ice-only condensate. The thick black curve is the angular momentum contour passing through the lower tropospheric location of maximum $\bar{v}$. (b) As in (a) but for a 6-h time interval centered 21 hours after t_*. (c,d) As in (a,b) but for simulation T28-HRA. (e,f) As in (a,b) but for simulation T30-HRA. The colorbar to the right is for all subfigures.

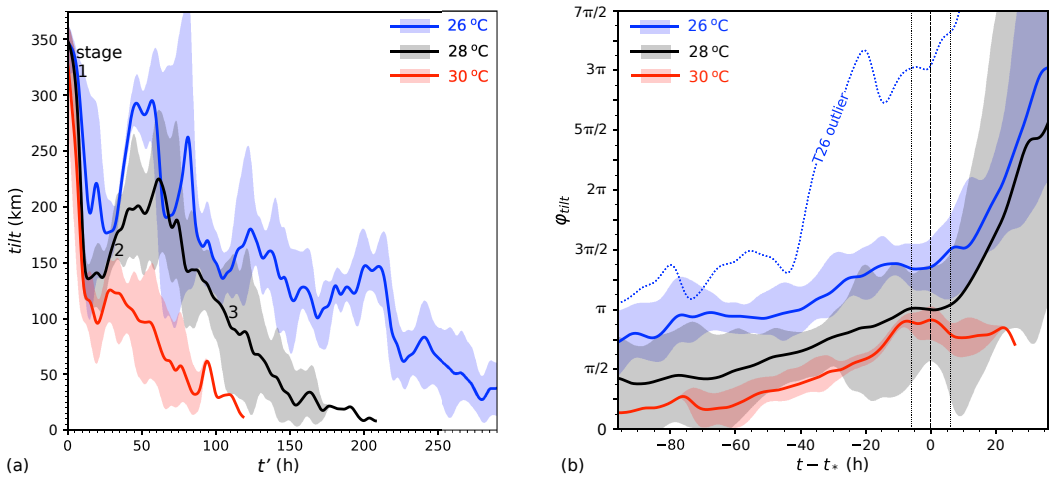

Figure C1: (a) Time series of the tilt magnitudes for tropical cyclones initialized with $318 \leq tilt_0 \leq 367$ km and $z_l = 5.25$ km. The thin-dark and thick-semitransparent curves represent the mean and spread of the time series in each SST group, as explained in the main text. The time coordinate used for the graph is defined by $t' \equiv t - t_0$, in which $t_0 = 0$ (6 h) for tropical cyclones initially tilted with the DSPD (IS or ISPD) method described in section 2b. The three stages of alignment are indicated in the general vicinities of where they occur for group T28. (b) The tilt angle φ_{tilt} versus $t - t_*$ for all tropical cyclones with well defined transition points during the HFP. The curves are as in (a), but an outlier (dotted blue line) is removed from the data determining the thin-dark and thick-semitransparent curves for group T26. The vertical black lines correspond to $t = t_*$ (dashed) and $t = t_* \pm 6$ h (dotted).